Available online at www.sciencedirect.com

ScienceDirect

Advances in Space Research xx (2024) xxx-xxx

ADVANCES IN SPACE RESEARCH (a COSPAR publication)

www.elsevier.com/locate/asr

Remote Sensing of Electron Precipitation Mechanisms enabled by ELFIN Mission Operations and ADCS

Ethan Tsai[a,*], Akhil Palla[a], Austin Norris[a], James King[a], Cindy Russell[a], Sophie Ye[a], Jiashu Wu[a], Jason Mao[a], Sharvani Jha[a], Chanel Young[a], Graham Wing[a], Kevin Lian[a], Aiden Szeto[a], James Shiffer[a], Rishi Sankar[a], Kaivalya Tota[a], Annie Liu[a], Derek Lee[a], Uma Patil[a], Isabella He[a], Jonathan Tam[a], Alex McDermott[a], Katrina Le[a], Suyash Kumar[a], Kelly Nguyen[a], Michelle Nguyen[a], Chen Yap[a], Erica Xie[a], James Tseng[a], Laura Iglesias[a], Alexandra Roosnovo[a], Wynne Turner[a], Reed Curtis[c], Colin Wilkins[a], Emmanuel Masongsong[a], Ryan Caron[a], Xiao-Jia Zhang[b], Anton Artemyev[a], Vassilis Angelopoulos[a]

[a] *Department of Earth, Planetary, and Space Sciences, University of California, Los Angeles, Los Angeles, CA, USA*
[b] *Department of Physics, University of Texas at Dallas, Address, Richardson, TX USA*
[c] *Nyheim Plasma Institute, Drexel University, Address, Camden, NJ USA*

Received 1 May 2013; Received in final form 10 May 2013; Accepted 13 May 2013;
Available online 15 May 2013

Abstract

The Electron Loss and Fields INvestigation (ELFIN) mission comprising two 3U+ CubeSats was developed, built, and operated by several generations of undergraduate students at UCLA. The spin-stabilized CubeSats (spin-rate: 21 RPM) produced high-resolution measurements of precipitating, trapped, and backscattered fluxes of electrons and ions in the radiation belts. Launched in September 2018, ELFIN operated successfully until its deorbit just over four years later. At first, however, mission operations was very challenging and only tapped the full mission potential after a thorough redesign of the operations paradigm. This mid-mission adjustment yielded the higher data downlink volume necessary to acquire a comprehensive data set, therefore enabling ensemble studies with sufficient statistical significance. The new operational framework also led to additional improvements across the mission. Most notably, the Attitude Determination and Control System (ADCS) benefited from more reliable collections of magnetometer data for attitude determination, enabling knowledge and control to $< 1^{\circ}$. This allowed high pitch-angle resolution (especially within the loss cone) and high energy resolution spectrograms, both powerful diagnostics of radiation belt electron and ion precipitation. This paper highlights the scientific advancements made possible by ELFIN's efficient mission operations and ADCS design, unique for CubeSats, and emphasizes the role of electron precipitation measurements for future studies in magnetospheric, ionospheric, and atmospheric physics.

Keywords: ELFIN; CubeSats; radiation belts; electron precipitation; wave-particle interactions; magnetospheric physics

*Corresponding author: ethantsai@ucla.edu

https://dx.doi.org/10.1016/j.jasr.xxxx.xx.xxx
0273-1177/

1. Introduction

1.1. Motivation for ELFIN

Earth's magnetic field traps energetic particles in large toroidal regions around Earth known as the radiation belts. Energetic (often relativistic, with energy > 500 keV) electrons there are highly dynamic, with fluxes that can vary by five orders of magnitude on timescales from days to minutes (Horne et al., 2007). Such electrons can pose a risk to spacecraft and astronaut safety and are studied under the general domain of "space weather" (Horne et al., 2013; Baker et al., 2017). Energetic electrons (> 100 keV) can leave the radiation belts either by transport (back out into the magnetosphere and solar wind) or diffusively (via wave-scattering along the field line, leading to precipitation and loss through collisions with the denser atmosphere at ~ 100 km). Precipitation, often correlated with auroral phenomena (e.g., Miyoshi et al., 2020, 2021; Shumko et al., 2021), can cause many changes in the atmosphere (Tesema et al., 2020; Mironova et al., 2019; Chapman-Smith et al., 2023) and ionosphere (Oyama et al., 2017; Yu et al., 2018; Verronen et al., 2021), and is therefore also important to study from the perspective of atmospheric energy input. For example, higher energy electrons penetrate deeper into the atmosphere (Xu et al., 2020) contributing to localized ozone depletion (Thorne, 1980; Lam et al., 2010; Turunen et al., 2016) and, if they reach low enough altitudes, can even produce secondary ionization effects via bremsstrahlung radiation (Xu et al., 2021; Xu & Marshall, 2019). Energetic particles typically precipitate by two different mechanisms in Earth's magnetosphere: field-line curvature scattering (e.g., Sergeev et al., 1983, 1993; Yahnin et al., 2016) and wave-particle interactions (e.g., Thorne, 2010; Li & Hudson, 2019). In particular, energetic ion motion is largely controlled by the geomagnetic field configuration and Ultra-Low-Frequency (ULF; < 1 Hz) dynamics, whereas the smaller and more magnetized energetic electrons are mostly affected by electromagnetic waves within the Extremely Low Frequency (ELF) and Very Low Frequency (VLF) ranges ($10 - 10^4$ Hz) (Lyons & Williams, 1984). Prior to the launch of ELFIN, there remained many open questions regarding the nature and dynamics of electron energization or losses, both of which are currently still highly unpredictable during some of the most active magnetospheric phenomena such as geomagnetic storms and substorms. These phenomena are crucial for space weather forecasting, which aims to protect society from the harmful effects of these relativistic particles. Therefore, energetic electron precipitation during storms and substorms is intently studied by a wide range of space weather missions.

Most recent and current missions have been dedicated to exploring the radiation belts from an equatorial vantage point due to the prevalence of magnetospheric processes detectable at those high altitudes. At the equator, the range of pitch-angles (angle between particle velocity and background magnetic field) for particles capable of reaching the ionosphere (i.e., those within the loss cone) is very narrow (less than few degrees). However, the loss cone becomes large along the field line at low altitudes (several hundred kilometers). From such low altitudes (i.e., high latitudes along the field line), precipitation and associated losses can be well-characterized. When data are acquired there as a function of activity and MLT, statistical investigations of the drivers of precipitation are possible. This cannot be achieved with short-lived balloon or sub-orbital rocket flight(s), but instead requires long-lived LEO satellites acquiring high-quality measurements with significant throughput.

The Electron Loss and Fields INvestigation (ELFIN) is a space weather mission specifically designed to fill this observational gap (Angelopoulos et al., 2020). The mission consists of two 3U+ CubeSats that were developed, built, and operated by several generations of undergraduate students at UCLA. Both CubeSats launched together on September 15th, 2018 into a ~460 km circular polar orbit with a 93° inclination. After 4 dutiful years on orbit, ELFIN-A re-entered on September 17th, 2022 and ELFIN-B re-entered on September 30th, 2022, thereby concluding the operational phase of the mission. ELFIN was designed to capture, for the first time, the energy distributions of energetic electrons and ions (E > 50 keV) with pitch-angle (α) resolution high enough

to resolve the bounce loss cone (particles with pitch-angles within the loss cone ($\alpha < \alpha_{lc}$) are lost within one bounce period). Its primary objective was to determine the storm-time particle precipitation rates and elucidate the variety of different mechanisms that can lead to such particle losses. ELFIN accomplished this using an Energetic Particle Detector for Electrons and Ions (EPDE, EPDI)—capable of measuring the energy and pitch-angle distributions of energetic electrons and ions with $\Delta E/E = 40\%$ across 16 energy channels between 50 keV and 5 MeV—along with a Fluxgate Magnetometer (FGM) deployed at a distance of ~75 cm to avoid noise from the spacecraft bus. By spinning at just over 21 revolutions per minute (spin period ~ 2.8 sec) with its spin plane aligned with the orbital plane (to include the magnetic field direction), ELFIN's 16 sectors per spin yielded a spin phase resolution of $\Delta\alpha = 22.5^\circ$ and allowed for full pitch-angle coverage with sub-loss cone resolution. From its low-altitude vantage point, ELFIN routinely turned ON its instruments to collect data multiple times per day as it traversed the L-shell ranges $3 < L < 18$, providing a radial snapshot of equatorial processes at a given magnetic local time (MLT) in what were called "Radiation Belt Crossings", or "Science Zones" (SZs). The latter term, which is most commonly used, signifies that each collection captures much more than the outer radiation belt, including the slot region and parts of the inner belt on the low-latitude side, and the plasma sheet and parts of the polar cap on the other.

This was unique because no previous mission had been able to achieve such routine, high-recurrence rate, high-time resolution, high-energy, and high-pitch-angle collections of particle distributions within the radiation belts. The loss cone within these SZs was $\alpha_{lc} \approx 65^\circ - 70^\circ$—whereas it is usually $< 3^\circ$ at the equator—so equatorial missions, like the Time History of Events and Macroscale Interactions during Substorms (THEMIS) (Angelopoulos, 2008), Magnetospheric Multiscale (MMS) (Burch et al., 2016), and Van Allen Probes (VAP) (Mauk et al., 2013) cannot resolve the loss cone, let alone any spectral details inside or outside of it. Although equatorial, the Exploration of energization and Radiation in Geospace (ERG) (Kasahara et al., 2018) mission has the ability to measure precipitating electrons from the equator with high pitch-angle resolution; such electron precipitation measurements, however, are limited in energy to < 100 keV (Kasahara et al., 2018). This does not allow for the study of how particles can be accelerated to relativistic energies and how off-equatorial processes may affect precipitation rates. There have been a number of low-altitude missions in orbits similar to ELFIN's—such as SAMPEX (Baker et al., 1993), POES (Evans & Greer, 2004), and Firebird II (Crew et al., 2016)—none of which can provide either adequate/consistent pitch-angle resolution or the appropriate energy range in order to study the full gamut of energetic electron precipitation phenomena. The ability of ELFIN to measure precipitating, trapped, and reflected populations of particles in a single spin (in addition to pitch-angle distributions *within* the loss cone) provided the necessary capability to determine signatures of various types of wave-particle interactions. Every aspect of the ELFIN mission was optimized for this purpose, leading to the implementation of a CubeSat with a highly customized yet efficient design.

1.2. ELFIN System Overview

An expanded schematic view of ELFIN can be seen in Figure 1. The ELFIN payload consists of three primary instruments: (1) an energetic particle detector for electrons (EPD-E) and an energetic particle detector for ions (EPD-I) and (2) the fluxgate magnetometer (FGM). The avionics unit is comprised of 8 PCBs and 4 Li-Ion batteries stacked inside of a PEEK (Polyether Ether Ketone, a type of thermoplastic) frame with a thin aluminum and MLI (Multi-Layer Insulation) blanket shielding for electrical and thermal purposes. The flight computer (FPCB), attitude control board (ACB), and two solar-battery boards (SBPCB) were built by the Aerospace Corporation. Each board contains one or two PIC microprocessors with custom software and firmware implemented by UCLA students. Interface and auxiliary boards were also designed and built at UCLA, including two Little Et Cetera boards (LETC1 and LETC2), a big Et Cetera board (BETC), and various small PCBs for battery heaters and harness interconnects. The

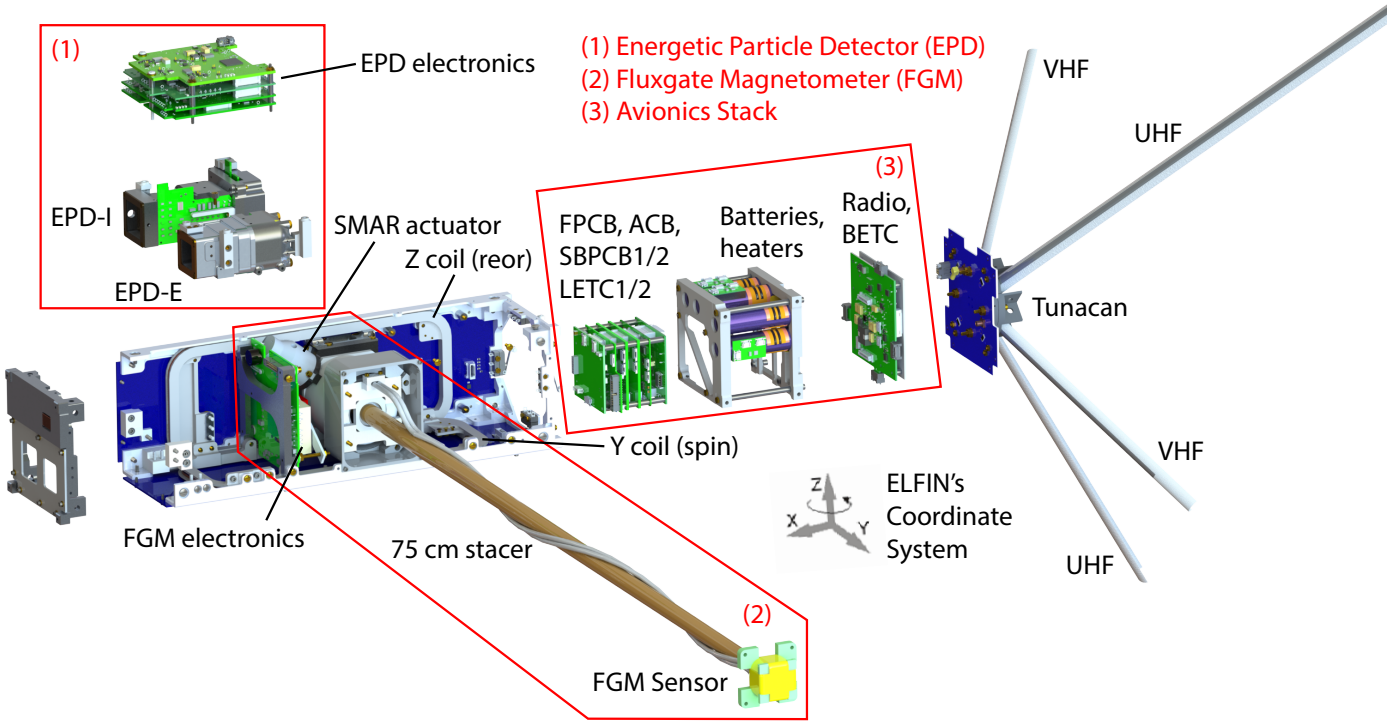

Fig. 1. Interior components of ELFIN are shown in this expanded view. From left to right: (1) the energetic particle detector instrument (EPD) which includes the electronics (SIPS, IDPU, 2 EPD digital boards, preamplifier, and the front end bias supply) along with the electron and ion sensor heads; (2) the fluxgate magnetometer (FGM) sensor mounted at the end of a 75 cm deployable stacer; and (3) the avionics stack which consists of the flight computer, solar battery power boards, attitude control board, radio, and relevant interface boards. The two pairs of deployable bent-dipole antennas are shown on the right, with the two air coils attached to the chassis. Note the coordinate system which is atypical from the CubeSat standard: ELFIN spins about its Z-axis, deploys the fluxgate in the +Y direction, and measures incoming particles from its +X direction.

radio is a custom form factor Helium-82 radio from AstroDev— which is a slightly smaller version of the Helium-100—capable of VHF uplink and UHF downlink. Power was generated via 20 body-mounted Spectrolab UTJ cells on custom solar panels and stored in 4 Molicel ICR18650J Li-Ion batteries.

There are two deployables on ELFIN: the antennas and the stacer boom. The antennas are stowed in the "bonus" volume of the 3U+ form factor, and consist of custom rolled up BeCu/fiberglass elements (built by Loadpath) held down by Spectraline as shown in Figure 2e. Deployment occurs when a series of redundant burn resistors are energized, which heat and melt the thin Spectraline and allow the antennas to unfurl. The stacer boom is a miniaturized version of the axial booms that were flown on THEMIS (designed and manufactured by Kaleva Design) and is pictured at the center of Figure 2a. The chassis and rail-based mechanical structure were custom designed and machined in-house. Most components were manufactured at UCLA with 6061 aluminum or PEEK (although brass, copper, tantalum, delrin, and Windform were either machined in-house or printed at commercial facilities). The magnetorquers were PEEK-framed air coils wound with Elektrisola High Tension Copper-Clad Aluminum (HTCCA) magnet wire, seen in Figure 2b. This magnet wire was chosen as an optimal compromise between resistivity, weight, and high tensile strength.

High-fidelity thermal simulations were performed in Thermal Desktop and validated by tests in our Thermal Vacuum (TVAC) chamber. These simulations informed the placement of various thermal treatments and blankets employed throughout the spacecraft. Custom MLI blankets, silver telfon, black kapton, and innovative use of PEEK brackets can be readily seen throughout Figure 2 and were designed to keep the EPD as cold as possible while minimizing battery heater use to optimize power utilization.

In addition to the standard challenges of miniaturizing three instruments, electronics, and deployables into a 3U+ CubeSat form

Fig. 2. ELFIN's flight model from various perspectives using axes defined in Figure 1.

factor, ELFIN's science goals imposed some unique challenges. First, by spinning at ~21 RPM with the spin plane aligned with the orbital plane to within 20°, ELFIN needed a custom ADCS solution, communication design, and power strategy. Second, due to the sensitive fluxgate magnetometer onboard, the spacecraft was required to be magnetically clean (<30 nT DC field @ 75 cm away): this limited material and design choices while also adding several levels of intricacies during system-level testing. Finally, the spacecraft was designed and built by a large team of nearly 300 undergraduate students across the 5-year development period while its on-orbit satellite operations was conducted by more than 50 undergraduate students over 4 years. This meant that retaining internal knowledge and enforcing high technical standards was a significant management-level challenge. The development, fabrication, testing, and satellite operations necessarily revolved around the academic calendar, which was an obstacle both to development continuity and to attaining reliable daily operations. There could not be an expectation of full-time commitment, and ELFIN's success relied heavily on extracurricular student volunteer time.

Operational Period	Time Range	Total SZ Crossings	SZs/Month
Commissioning	Sept 2018 - March 2019	0	0
Calibration + Ops 1.0	April 2019 - June 2020	675	~40
Refactor 2.0	June 2020 - Feb 2021	3255	~360
Inner Belt Observations	Mar 2021 - Nov 2021	5436	~600
Working Attitude Control	Dec 2021 - May 2022	2558	~380
Calibrated Ions	June 2022 - Sept 2022	481	~120
		Total: ~12,500	

Table 1. This table shows the various phases within ELFIN's on-orbit operations. The mission reached a turning point in June 2020 with the release of Refactor 2.0, which greatly enhanced the scientific return from ELFIN. Only observations in which data completeness > 60% over the planned *L*-shell range are counted (outer radiation belt crossings are from $L \in [3, 18]$ while inner radiation belt data collections span $L \in [1.1, 18]$).

1.3. Organization

This paper is organized as follows: Section 2 describes the operational performance over the lifetime of ELFIN and identifies satellite operations refactoring as pivotal to ELFIN's success. This is followed by a discussion of ELFIN's coverage from a space physics perspective in Section 3; this extensive coverage is only enabled by a comprehensive overhaul of satellite operations, called Refactor 2.0, described next in Section 4. Refactor 2.0 also led to better attitude control, which is covered in the context of satellite operations in Section 5. The novelty of obtaining pitch-angle-resolved electron distributions in low Earth orbit (LEO) afforded by functioning attitude control is detailed in Section 6. In Section 7, we discuss the overarching strategies and lessons learned relevant to small satellite capacity building, look ahead to the possibility of future missions, and emphasize the value of contextualized electron precipitation measurements. Further technical details regarding the implementation of Refactor 2.0 and ELFIN's ADCS design are found in Appendix A and Appendix B.

2. Operations Timeline

ELFIN data has enabled a wide range of studies primarily due to its novel data products, multi-year statistics, full MLT coverage, and thousands of science zone (SZ) data collections. Effective satellite operations and full attitude control were the two final hurdles that were overcome on-orbit which enabled the necessary throughput of high-quality science data.

One metric for assessing ELFIN's data throughput (and, therefore, operational success) is the number of SZs ELFIN successfully downlinked per month, as itemized throughout various phases of ELFIN's on-orbit life in Table 1. Even after commissioning, the first two years were challenging: more than 95% of the $12,500$ science zone crossings were downlinked by ELFIN after the first 1.7 years of the mission, i.e., after a complete revision of its operational paradigm, called Refactor 2.0, was rolled out in June 2020. This is shown in the last column of Table 1. It can be seen that the ELFIN SZ downlink rates improved by 9x after this refactoring and remained sustainably high until the end of the mission. This rapid increase in downlink data volume is also evident in Figure 3. Science zone downlink efficiency after Refactor 2.0 fluctuated as a function of partner downlink station availability (partners included NASA's Near-Earth Network (NEN) dish-antenna on Wallops Island, StellarStation's antennas in Tokyo, and Montana State University's UHF downlink station). It also fluctuated due to downlink complications from ELFIN overlapping passes (or OLPs, when both ELFINs are overhead during the same passes, effectively halving the available pass time), and additional desired data volume per science zone collection (SZs/month decreased when downlinking additional inner belt data, attitude data, and/or ion data corresponding with each of ELFIN's more advanced operational phases). It took several months to optimize our operations paradigm around the new software, and our first major update (which included significantly more optimized science packets and better downlink strategies) was released shortly before the first set of overlapping passes at the

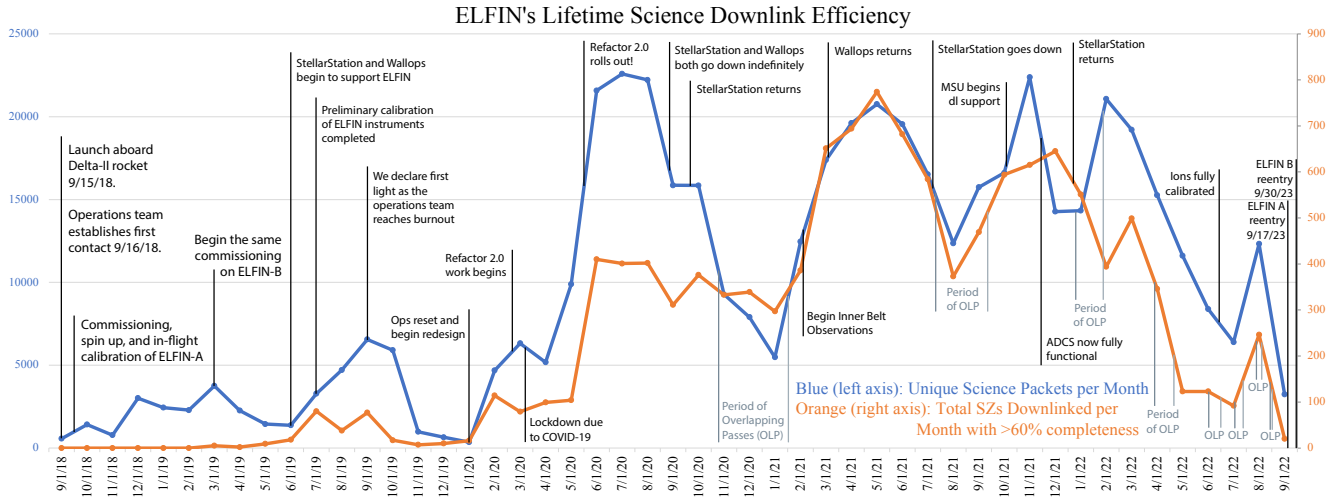

Fig. 3. We show ELFIN's science packet downlink efficiency (blue, left axis), measured in science packets downlinked per month, as well as science zone downlink efficiency (orange, right axis), measured in number of science zone crossings with greater than 60% completeness per month. Key phases of the mission are annotated, showing the large impact of Refactor 2.0 and how it enabled significantly higher cadence and coverage of ELFIN measurements. Various effects cause the downlink efficiency to vary throughout the mission, such as variable external downlink support and increased downlink volume requirements to support new science/operations objectives.

end of 2020. This significantly reduced the error rate at which we downlinked data, as exemplified by the closer matching slopes between the blue curve (the total number of science packets downlinked, including duplicates) and the orange curve (the total number of SZs downlinked with completeness > 60%). When ADCS became fully operational in November 2021—demonstrating attitude determination and control of both ELFINs to $< 1^\circ$ of precision—it significantly increased the quality of ELFIN science data at the cost of reduced overall science data due to the increased attitude data downlink requirements and even more constrained spacecraft resources. Combined with ion data becoming fully online in June 2022—which increased generated data volume per SZ by 50%—and the rapidly increasing OLPs, the number of SZs downlinked decreased towards the end of the mission. The lower SZ coverage manifested near the end of mission was justified by the added value of fully contextualized ELFIN data with all instruments working, allowing ELFIN to achieve far more than its originally proposed science objectives.

3. ELFIN Data Coverage

ELFIN was inserted into a circular 460 km orbit with 93° inclination. This results in just under 0.5° of nodal precession per day, meaning that the orbital plane rotates about 180° in a year (relative to the Sun-Earth system), and, given the freedom to chose any of the four available science zones in each the orbit (at opposing meridians), results in full MLT coverage once per year. With the increased science collections afforded by the refactored satellite operations, each ELFIN satellite was collecting and downlinking up to 12 SZs per day, depending on power constraints and downlink backlog. Figure 4 shows the lifetime ELFIN coverage as a function of MLT and geomagnetic indices. ELFIN lifetime coverage per MLT sector (indicated in (d) by light blue bars and numbers) show reduced coverage near midnight because the noon-midnight orbit case is ELFIN's coldest and lowest power state (given its attitude requirement of having the spin axis along the orbit-normal). Not only are Earth shadows maximum here (ELFIN charges for only over half its orbit track), but also panels along ELFIN's spin plane have reduced solar cell coverage since instruments and deployables are also in the same plane. This results in reduced power availability for downlinks and lower SZ collections in the noon-midnight meridian, as evidenced in the figure.

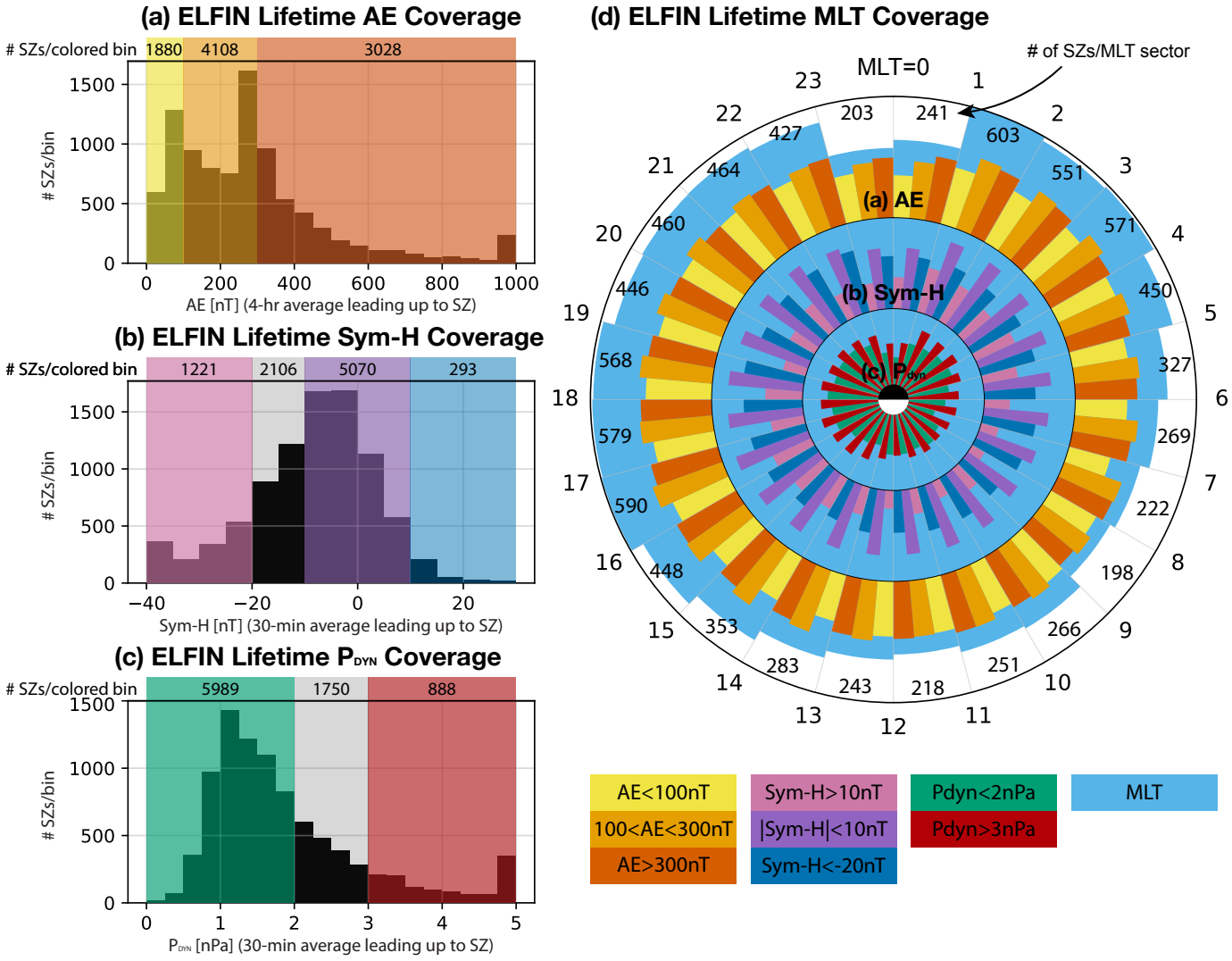

Fig. 4. ELFIN lifetime coverage binned by (a) auroral electrojet (AE), (b) high resolution Dst (Sym-H), and (c) solar wind dynamic pressure (P_{dyn}) levels (King & Papitashvili, 2005). (d) shows lifetime MLT coverage in light blue, while each ring indicates the different levels/states of activity/magnetosphere per MLT sector based on color coding indicated at the bottom right. Geomagnetic indices used here are averaged over 4/0.5/0.5 hours leading up to each science collection; AE indicates substorm activity with quiet/moderate/active corresponding with yellow/orange/dark orange; Sym-H indicates storm activity and ring current strength, with compressed magnetosphere/quiet geomagnetic activity/active geomagnetic activity corresponding with pink/purple/blue; P_{dyn} indicates the dynamic pressure of the solar wind on the magnetosphere, with larger values (red) indicating strong magnetospheric compression.

The data is further binned as a function of three geomagnetic indices, mean AE (averaged over 4 hours prior to the SZ), Sym-H (Dst), and P_{dyn} (both of which are averaged over the 30 minutes prior to the SZ). Figure 4(a-c) show coverage binned by magnetospheric conditions. Although most of the time the magnetosphere is quiet, exhibiting low substorm activity (yellow, with AE < 100 nT), Figure 4a shows that ELFIN made the vast majority of its collections at times of moderate geomagnetic substorm activity (orange, with 100 < AE < 300 nT). This is because when storms (generally including multiple intense substorms) were forecast or ongoing (based on Kp and AE indices), operators would schedule more science collections than normal, meaning that ELFIN's AE coverage does not represent the actual statistical AE occurrence. This can be seen by an unnatural peak in the histogram at about AE~250 nT and a general skew of collections preferentially towards active times (dark orange, with AE > 300 nT). Such collections provided the desired abundance of collections during periods of strong plasma injections with intense wave activity.

Figure 4b shows ELFIN coverage binned by Sym-H (minute resolution ring current index, Dst), where most measurements are made under quiet-time magnetospheric conditions (purple, |Sym-H| < 10 nT). There is fair coverage when Sym-H < −20 nT (pink), which represents pronounced ring current and plasma sheet (ion and electron) injections, typically associated with EMIC wave-induced electron precipitation in addition to storm-time electron acceleration and pitch-angle scattering by whistlers.

Figure 4c shows ELFIN coverage binned by P_{dyn}, the solar wind dynamic pressure on Earth's magnetosphere. The majority of SZs are collected during non-compressed magnetospheric conditions (green, with $P_{dyn} < 2$ nPa). However, there is sufficient coverage during compressed magnetospheric conditions (red, with $P_{dyn} > 3$ nPa) when dayside drift shell splitting and magnetopause shadowing effects are more pronounced, allowing for studies of geomagnetic field topology effects on electron anisotropy, wave generation, wave-scattering, and subsequent precipitation.

There are a total of 9,200 SZs included in Figure 4, which is fewer than the 12,500 SZs mentioned above in Section 2 because the criteria used here are stricter: we excluded all data that is (1) collected in the South Atlantic Anomaly (SAA), (2) contained low precipitation/count rates, or (3) contained any significant data quality issues. Conversely, including all ELFIN data without any restrictions results in a much larger number of SZs downlinked: around 20,000 SZs. Although many of these collections have data gaps, they are still usable (e.g., Tsai et al., 2023; Tsai et al., 2024, statistically analyzed ELFIN data at the spin level).

ELFIN's large coverage of MLTs and geomagnetic conditions enables studies which can statistically characterize various types of wave-particle interactions (e.g., Angelopoulos et al., 2023; Capannolo et al., 2023; Tsai et al., 2023; Tsai et al., 2024; Zhang et al., 2022a), compare electron lifetimes in the radiation belt with models (Mourenas et al., 2021, 2024), and investigate phenomena such as isotropy boundary properties and their dependence on activity and longitude (Wilkins et al., 2023). Additionally, ELFIN's spatially and geomagnetically comprehensive collections yield increased opportunities for active time conjunction studies with other spacecraft and ground-based observatories (see examples of such studies in Chen et al., 2022; Grach et al., 2022; An et al., 2022; Gan et al., 2023). In particular, ELFIN and THEMIS (Angelopoulos, 2008) coordinated their collections to make multiple daily measurements when ELFIN's orbital plane aligned well with either THEMIS' inbound or outbound leg of its orbit through the inner magnetosphere. As shown in Figure 5, by deliberately including, in a similar fashion, conjunctions with other observatories whenever it was opportune to do so (ERG (Kasahara et al., 2018), MMS (Burch et al., 2016)) and by the sheer volume of data enabling conjunctions with GPS (GPS53–73, excluding 60) (Distel et al., 1999; Morley et al., 2016, 2017), and DMSP (DMSP15-18) (Hardy et al., 1984; Greenspan, 1986; Rich & Hairston, 1994) satellites, we find that ELFIN has obtained thousands of high-quality conjunctions (fairly strict criteria of ΔMLT < 1 and ΔL < 1) with other missions. By relaxing the conjunction constraints, either spatially or especially temporally, the number of conjunctions available for study grows substantially. In terms of ground station coverage, many ELFIN collections were preferentially planned with their ionopsheric footprint over North America/Canada, so a large fraction of SZs additionally coincide with all-sky imager and ground magnetometer coverage.

Spacecraft conjunction coverage as a function of L and MLT is shown in Figure 5a, where conjunctions with equatorial spacecraft here are defined as any high-quality SZ within ΔMLT < 1 and ΔL < 1. This comprehensive coverage with equatorial missions provides key wave and particle inputs, enabling a large number of case studies to be performed. For example, Artemyev et al. (2021, 2024a) confirmed that ducted whistler-mode waves are likely a significant contributor to relativistic electron losses using ELFIN, in conjunction with ground VLF receiver stations and equatorial spacecraft measurements. Tsai et al. (2022) showed that THEMIS wave and plasma measurements, when modeled, produced a precipitation distribution closely matching ELFIN observations, while Gan et al. (2022) used several events of ELFIN-THEMIS conjunctions to provide the first direct evidence of high-order resonance-driven relativistic electron precipitation. Angelopoulos et al. (2023) and Grach et al. (2022) utilized ground-based EMIC

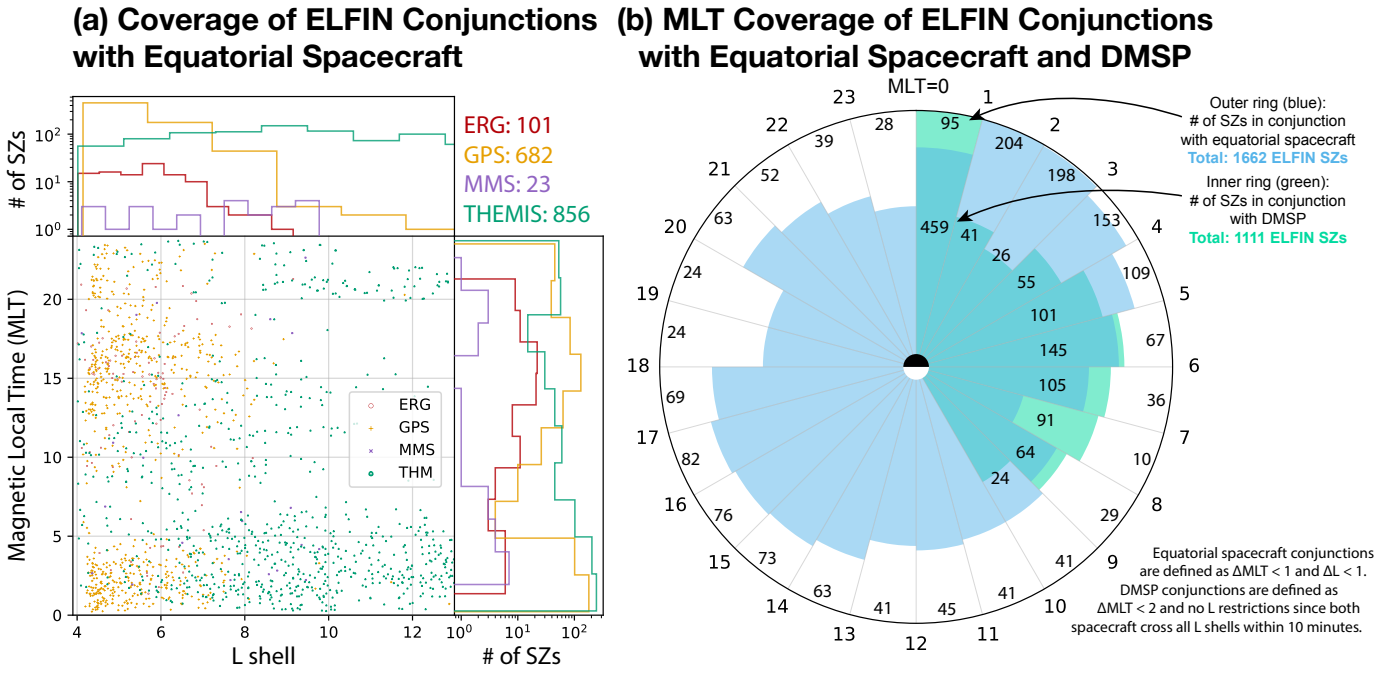

Fig. 5. Lifetime ELFIN conjunctions with 4 equatorial missions (ΔMLT $<$ 1 and ΔL $<$ 1) are shown geographically in (a) as a function of L shell and MLT with corresponding histograms in log scale. These are further binned by MLT sectors in (b), with the blue bars and outer numbers indicating total equatorial spacecraft conjunction events in each MLT sector. The green bar and inner numbers indicate ELFIN conjunctions with the polar orbiting DMSP spacecraft defined as ΔMLT $<$ 2. There are more conjunctions with other missions and ground stations not shown here.

measurements to explain ELFIN-observed relativistic electron losses, while Capannolo et al. (2023) differentiated between relativistic electron precipitation driven by EMIC waves versus curvature scattering using ELFIN-conjunctions with ring-current ion precipitation observations from POES. Sergeev et al. (2023) combined ELFIN precipitation measurements with near-equatorial THEMIS data to construct a detailed magnetic field model of substorm dynamics. Notably, two new mechanisms of bursty, sub-relativistic electron precipitation were discovered using multiple conjunctions of ELFIN with near-equatorial measurements of very oblique whistler-mode waves: nonlinear Landau trapping (Artemyev et al., 2022b) and loss-cone overfilling (Zhang et al., 2022b).

Figure 5b also includes DMSP conjunctions (green bars), polar-orbiting spacecraft capable of measuring the thermal population of electron precipitation in a mostly noon-midnight sun-synchronous orbit. The conjunctions here are defined as collections within ΔMLT $<$ 2 of each other, regardless of dependence on L, since they both cross all L shells within 10 minutes of each other. DMSP-ELFIN conjunctions have already been used to study energetic electron precipitation embedded within sub-auroral polarization streams (SAPS) (Artemyev et al., 2024b) and energetic electron losses from plasma sheet injections (Shen et al., 2022b). These types of studies are only possible thanks to the extensive coverage ELFIN provided through the Refactor 2.0 effort, discussed below.

4. Refactor 2.0

4.1. Planner, Intents, and Allocations

The original operational design for planning and scheduling spacecraft activities was accomplished in the **Planner** software module. The original Planner had a timeline view which allowed the user to view all pertinent orbital events and add spacecraft activities as they desired. However, matching all these activities with resources used on the spacecraft was too complex to automate and was therefore done manually. As a result, this flexibility led to a complicated experience where operators were oftentimes juggling several tens of different activities daily, manually keeping track of how the state of each activity evolved over time and

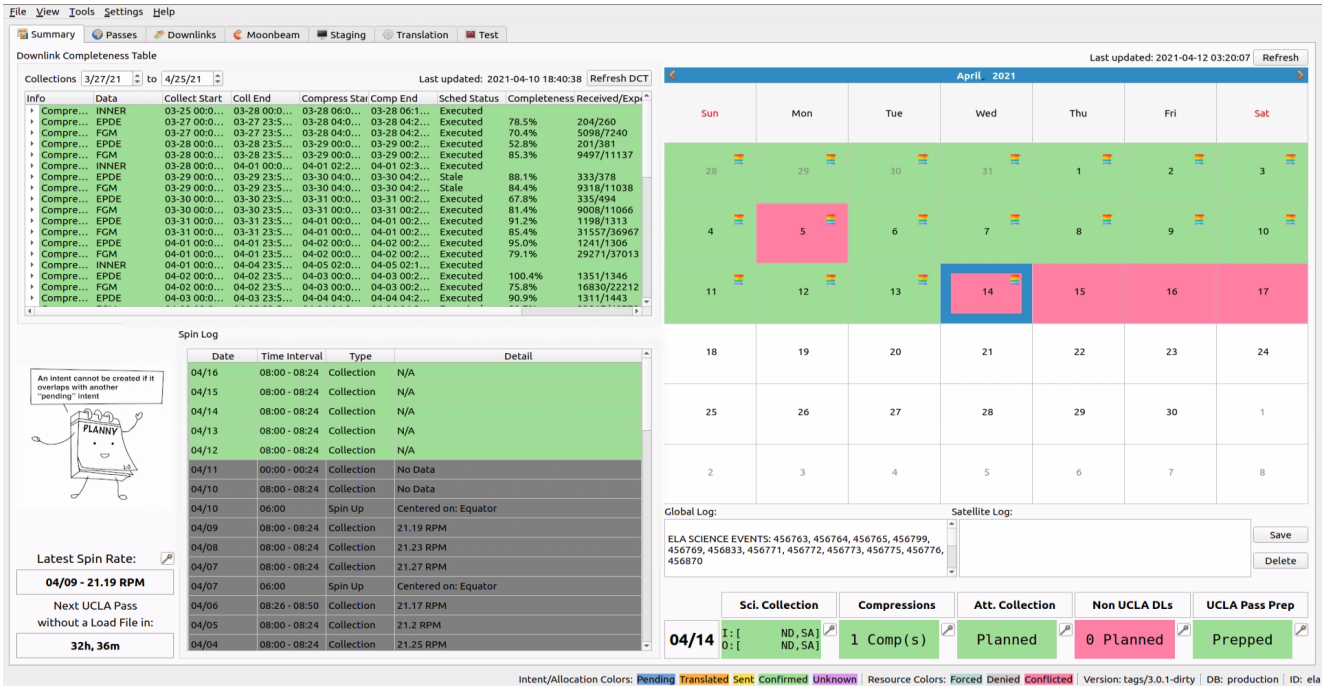

Fig. 6. A screenshot of the Planner in April 2021. In the calendar view, green denotes when all necessary Intents are confirmed aboard the spacecraft for that day. This allows operators to quickly tell which days and what activities have yet to be planned. Intent/Allocation states are color-coded on the bottom bar. Clicking on the "wands" will bring up Intent creation "wizards" for each type of Intent. Clicking on each day shows a summary of the Intents planned at the bottom right. The 14th is red because Downlinks Intents over non-UCLA stations have yet to be created. The Downlink Completeness Table (DCT) on the top left side provides up-to-date downlink completeness percentages and Intent states for each Science Compression Intent. Expanding each of those would show the associated downlink completeness and Allocation state for each of the associated science collections. The spin log on the lower left corner shows the latest spin rates.

figuring out each planned activity eventually mapped to spacecraft memory to determine where future activities could be stored. Thus, the operations team used several supplemental spreadsheets just to maintain updated status on daily operations; this tedious, time-consuming effort rapidly became untenable.

The refactored Planner (Figure 6) removed the timeline view, instead opting to build a new workflow around “wizards” (similar to generic software installation wizards) where the user interface would guide operators through a sequence of simple allowable steps, allowing them to plan each spacecraft activity while following a rigid set of rules that were enforced by the software logic in the background. Each spacecraft activity would be associated with an **Intent** – which refers to a high-level spacecraft activity, such as collecting science, performing attitude maneuvers, compressing science data, downlinking data over a communication pass, etc. Thus, each Intent would have its own dedicated wizard workflow. Intents carry all the information necessary to perform the particular activity in a human-readable format in addition to the **Scope**, which is the property that allows Intents to be compared to each other, thus allowing the software logic in the background to ensure that Intents do not overlap or conflict. Intents require onboard **resources** to be executable, such as flash memory space or scheduler space, that would dynamically change as a result of the intended flow of execution. The mapping from an Intent to a resource was defined as an **Allocation**. Thus, this paradigm would become known as the **Intents and Allocations** paradigm, because any activity onboard the spacecraft could be traced to an **Intent** (high level, human-readable information) and its associated **Allocation** (how this particular activity was to be executed on the particular spacecraft). A rigid series of rules and constraints was implemented in the background to keep operations safe and prevent unintended behavior: Intent rules were designed to ensure no conflict of activities and scheduling, while Allocation rules would ensure no conflicts onboard spacecraft resources. Further definitions and rules are detailed in Appendix A.

The eight different ELFIN Intents are as follows:

1. **Science Collection Intents** help ELFIN achieve the primary goal of the mission by enabling a specified mode of science collection across any number of Science Zones throughout an entire day. The wizard allows the operator to select any

Science Zone that does not conflict with any other intent. It would also display geomagnetic activity and highlighted periods of conjunctions with the THEMIS probes. In addition, the wizard would check the other ELFIN satellite's Science Collection Intents and highlight any SZ within 30 minutes of an already selected SZ. This enabled studies of the spatial and temporal evolution of kinetic scale to mesoscale phenomena, such as Zhang et al. (2023a).

2. **Science Compression Intents** were necessary for ELFIN to bring down the volume of science data generated since the data compression operation had to be commanded. This introduced a lot of hidden complexity, as there were many different types of science data, several options for data compression, and multiple compression timestamps associated with each data compression.
3. **Attitude Collection Intents** were nominally required every other day to assess the attitude (orientation) of the spacecraft. Attitude knowledge was accomplished by recording 24 minutes of 3.125 samples per second (SPS) magnetoresistive magnetometer (MRM) data (mounted on the electronics boards within the spacecraft-body) while avoiding terminator crossings (because the battery charging regulators produced random offsets in the MRM data that were difficult to calibrate out).
4. **Spin Maneuver Intents** were typically required twice a week to maintain ELFIN's desired spin rate. These were typically centered at the magnetic equator, where the B field magnitude is weaker and allowed for fine control of the spin rate.
5. **Reorientation Maneuver Intents** were typically required once a week to maintain ELFIN's attitude pointing. This was a ground-in-the-loop commanded maneuver involving a suite of software tools called *Attitools* (see Appendix B).
6. **Downlink Script Intents** were the only non-temporal intent, and allowed operators to select what data to downlink and store on an addressable script onboard the spacecraft. These scripts could then be used for downlink during UCLA (commanded) or non-UCLA passes (scheduled).
7. **UCLA Pass Prep Intents** were simple scripts that were scheduled before a communications pass over UCLA and ensured the spacecraft was set to a known consistent state and ready to downlink.
8. **Non-UCLA Pass Intents** performed the same activity as UCLA Pass Prep intents in addition to linking to a specified Downlink Script such that data was automatically transmitted over a non-UCLA ground station.

Most of these Intents have unique scheduling constraints, but we refrained from fully automating this in order to avoid hidden complexity. The goal was to deliberately balance what operators can and cannot control: automate too much and the system becomes a rigid black box that students have no ownership over; automate too little and the system becomes tedious, cumbersome, and error-prone. Thus, the compromise was that operators would select a time window (representing the scope of an intent) and the software would find the optimal time within the window to schedule something. For example, in the Spin Maneuver generation wizard, the operator would be presented with the historical trend of spin rates, a few options for configuring the spin control law, and a selection menu showing all valid 2-hr windows (the scope). Upon choosing a 2-hr window, the Planner will pick a time that centers the spin maneuver over the magnetic equator and on the next window, the user will select what scheduler address on the spacecraft to use. Therefore, a simple two-page wizard allows the operator to quickly create an Intent and Allocation in a traceable and conflict-free manner. Operators typically created 20-30 Intents per spacecraft per day, which would normally take about 30 minutes (including the next steps which involve translating the Intents/Allocations to commands and generating command load files). Prior to Refactor 2.0, operators would spend an average of 3 hours per spacecraft per day and achieve, at best, about 10 SZs per spacecraft per week. In the first month after the release of Refactor 2.0, operators were spending only 3 hours on console per spacecraft *per week* and downlinking nearly *50 SZs* from each ELFIN per week. By version 3.0 of the ELFIN operations software

(which notably enabled inner belt observations in March of 2021), the operations team achieved 75 SZs per spacecraft per week without spending more time: this is roughly a 50-fold efficiency increase compared to pre-Refactor 2.0.

4.2. Downlink Completeness Table

A major theme of the refactoring was providing contextually useful information. By taking advantage of the Intents/Allocations framework, we could track the state of Allocations from beginning to end, and therefore quickly understand the state of the spacecraft as a whole. The **Downlink Completeness Table** (DCT) integrated key aspects of the science data processing pipeline into the Planner and leveraged the new layered levels of insight afforded by the paradigm of Intents and Allocations in order to give operators direct access to information regarding collections of science data, onboard data processing/compression status, and downlink status/completion rates. The full view is accessed in the Downlinks tab in the Planner (not shown), but a smaller preview can be seen in the upper left side of Figure 6.

The DCT shows all science collections (based on Science Collection Intents), grouped into uncompressed and compressed (based on Science Compression Intents). This consolidation was already beneficial, as operators previously used spreadsheets to track the many different types of timestamps associated with each science collection: (1) the science collection date; (2) the n timeranges associated with the n planned science zone crossings throughout that given date; (3) the science compression timerange; (4) up to four science compression timeranges (one for each product: EPDE, EPDI, FGM, and inner belt data); (5) the downlink time (of which data is typically downlinked over 2-4 passes to ensure high completeness percentages). This quickly became confusing, as there was a fast-growing number of new timestamps required to keep track of command state and future command generation that was produced each day. The DCT was thus the cornerstone of the refactored Planner as it consolidated, grouped, and provided the status of every SZ ELFIN collected. By presenting the downlink completeness rates of each SZ, the operator could easily recognize which SZs needed the most attention; they could then map the desired data and timestamps to the Downlink Script Intent wizard without typing anything. As one of the largest sources of operator error came from manually typing timeranges and timestamps, completely avoiding that step (and minimizing typing in general) during planning operations saved time and ensured that every downlink worked as intended.

4.3. Management

Ultimately, ELFIN was a small student-driven development and satellite operations team. An oft repeated phrase in spacecraft engineering is to “push complexity to the ground.” In this case, however, a simple but flexible flight software design on ELFIN made satellite operations untenable, incurring significant team attrition and resulting in software that was incompatible with the team it was supposed to help. We recognized quickly that the solution was for the operations software design to focus on being as understandable and traceable as possible, prioritizing these facets at the cost of performance, flexibility, and other factors. Refactor 2.0 was a significant undertaking that vastly simplified the operational paradigm, despite growing the codebase to nearly half a million lines of code across 15 different custom software modules (see Figure A.13). However, there was also a big focus on layered code organization, which led to easier-to-maintain code and reduced troubleshooting times when issues arose. This gave both the operations and the software developers teams more time to tackle off-nominal operations and develop future improvements to the ground software.

Another key aspect of Refactor 2.0’s success was ensuring that workers and stakeholders were in constant communication. This was done by having developers regularly operate the spacecraft along with the dedicated spacecraft operators, forcing operators to present operational metrics to the science team weekly, and creating automated "tohban" (i.e., Autohban) reports (in the context

of prior science missions like RHESSI and THEMIS, this term refers to a person-in-charge, a scientist whose job is to check the science quality of observations and quickly notify the operations team if anything is amiss) that allowed scientists to quickly and consistently convey any issues to the student team through a standardized format. These combined decisions led to a positive feedback cycle that continually fixed operational problems by focusing on metrics, usability, and transparency. It formalized and standardized both operations and scientific oversight, leading to streamlined operations, rapid detection of any science quality issues, and allowed operators to focus on bringing down the most useful science data.

5. ADCS

The newly refactored operations afforded the team more time and data volume to begin improving other aspects of the mission by updating and expanding the Intents and Allocations framework. This quickly enabled an expansion of science scope as well, beyond the goals of the minimum mission (outer-belt electron collections). New targets included studies of the inner belt and doubling the pitch-angle resolution of the EPD collections (from 16 to 32 sectors per spin). After streamlining science operations, resources were then allocated to resolving two issues related to science objectives beyond minimum science: 1) fully calibrating the EPDI (ion) data (ion data is not discussed in this paper, but the data is shown in, e.g., Shen et al., 2023a; Artemyev et al., 2023, 2024b) and 2) improving the quality and flexibility of science zone collections by fixing ELFIN's ADCS.

ELFIN utilized a highly stripped-down ADCS architecture that relied on only one sensor and one pair of actuators. This is possible due to the spin-stabilization provided by the stacer boom, which damps rotation about other axes (wobble) other than the primary Z spin axis. Because ELFIN is spin-stablized, its attitude can be described by its spin axis vector in GEI (Geocentric Equatorial Inertial) in addition to its spin rate. Attitude determination is performed on the ground, utilizing data collected from a low-cost, but reliable 3-axis HMC5883L magnetoresisitve magnetometer (MRM). For redundancy, each ELFIN contained two MRMs placed on electronics boards on either side of the spacecraft. Spin rate was maintained at ~ 21.15 RPM with a magnetorquer, an air coil (along the Y face), using closed-loop B-act and B-dot algorithms. The former relied on applying a torque based on the **act**ual magnetic field, and reliably worked down to zero spin; the latter is widely used for detumbling spacecraft (Stickler & Alfriend, 1976; Lovera, 2015). On ELFIN, B-dot was tuned to control spin rates from 7-35 RPM, while B-act was slightly less efficient and designed to work at all spin rates. This worked well right from the beginning of the mission, immediately after launch, enabling early orbit operations. Spin control is described in more detail in Appendix B.

"Reorientations" (or "reors" for short), on the other hand, could not easily be tested at a hardware level on the ground and instead, verification relied on simulation for maneuver planning and validation on orbit. The spacecraft spin axis is precessed by pulsing the Z-coil at precise points in orbit when the magnetic field lined up in such a way that the torque generated would move ELFIN's spin axis towards its target vector. A reor would typically require four short ($1-5$ min) pulse sequences per orbit, where the duration of each pulse was determined by the error tolerance: longer pulses result in faster reors with lower precision. Nominally, ELFIN would perform $20-30^\circ$ reors over ~ 10 orbits with minute-long pulses to keep control precision well below 1°.

Reors, however, were difficult to verify on orbit due to our uncertainty in attitude determination, which arose from MRM offsets on the order of 1000 nT that changed every time the spacecraft was rebooted. This complicated attitude determination early in the mission, which was still possible assuming spin-axis evolution was changing slowly (which was the case in the absence of reor maneuvers). Therefore, as long as the spin vector was evolving not too far from orbit normal, lack of control did not affect science significantly. The EPDE data sectoring used the onboard FGM instrument while pitch-angle binning occurred on the ground; both were sufficient to satisfy the primary mission. As operations streamlining and high-science yield efforts took the

primary development focus initially, ADCS troubleshooting and development efforts were relegated to a lower priority. However, by mid-2021, attitude determination was revisited resulting in operational improvements, which eventually led to the successful implementation of full attitude control on both spacecraft by November 2021.

5.1. Attitude Determination

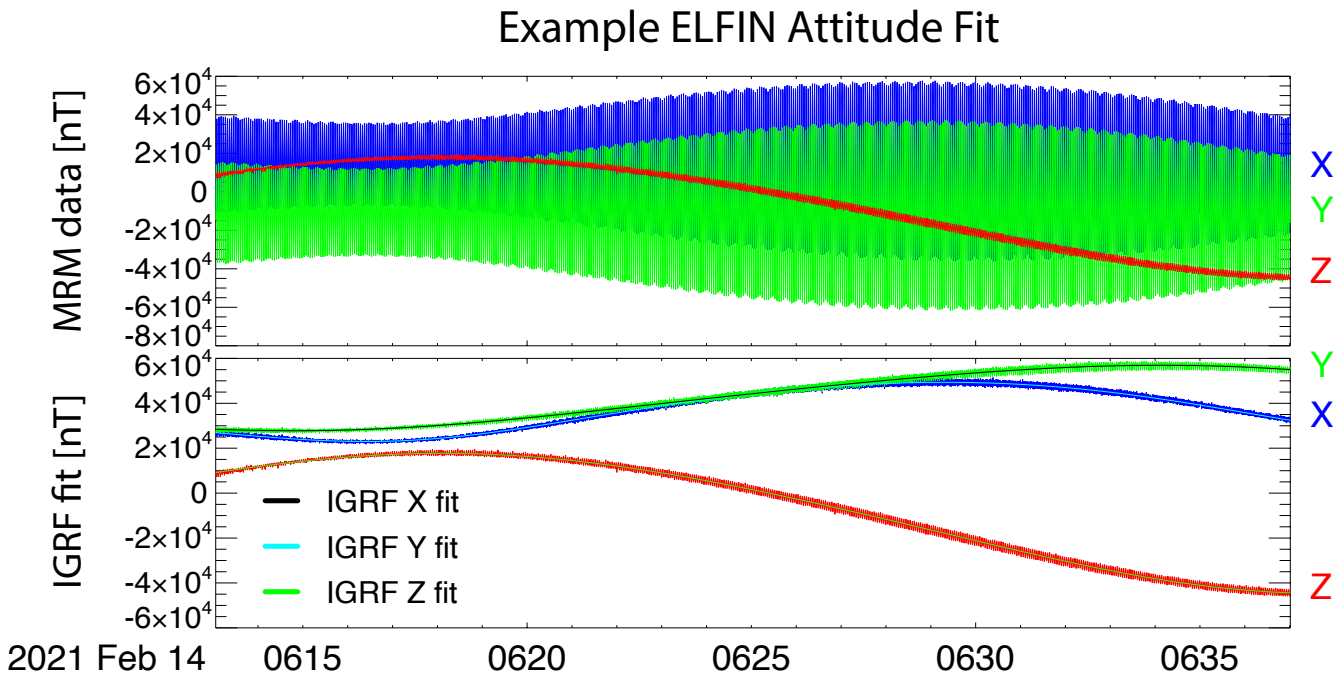

Fig. 7. Top panel shows a sample attitude collection (i.e., 24 minutes of MRM data collected at 3.125 SPS, in ELFIN body coordinates). ELFIN's attitude determination procedure finds the optimal attitude that fits the MRM data, including offsets and gains, to the IGRF field. Results of data and model fit are shown in the second panel in (despun) GEI coordinates.

To keep ELFIN capable of obtaining full pitch-angle resolution, ELFIN's spin plane must contain the local magnetic field vector within the EPD's 22.5° field-of-view (FOV). In a polar orbit, this could be more simply approximated as aligning the spin plane with the orbital plane. ELFIN nominally used 24-minute MRM collections (out of the ~ 90 minute orbital period), which provided sufficient field variance for the data to be fit to the IGRF model field. The attitude determination method was not very sophisticated at first, fitting only MRM offsets and using a blocked-bootstrap Monte Carlo simulation to check for stability. Therefore, attitude determination was unreliable with very high uncertainty (several degrees, yet still sufficient for EPDE science whose data was sectored relative to the zero-field crossings using the FGM). For purposes of ADCS, though, this condition meant that we could only determine the spacecraft attitude with reasonable fidelity when it drifted consistently (especially assisted by using historical sine fits), but had difficulty acquiring the absolute orientation value again after attitude reorientation maneuvers, due to abrupt changes in attitude. Thus, for a large portion of the mission, operators refrained from performing reors. Rather, they planned to acquire data during the best one or two out of the four possible SZ collection opportunities per orbit that minimized the angle between B and the spin plane. These were found by checking when the quadrants in which the B-to-spin-plane angle is minimized, simply due to Earth's tilted dipolar field. This operations paradigm in the early part of the mission resulted in reasonable-quality collections, i.e., having good pitch-angle coverage within the loss cone. While not ideal, it served the science sufficiently well until fully functional attitude determination and control was enabled in November 2021. Once ADCS control was fully functional, it

meant that both ELFIN satellites could measure across any of the four available SZ crossings with full pitch-angle coverage and resolution within the loss cone. This qualitative improvement in the science enabled a wealth of new studies which are detailed in Section 6.

ELFIN's ADCS software was built into a software module called **Attitools**, which bridged functionality between IDL code (for attitude determination), Julia code (for attitude modeling), and Python code (for integration into ground operations and science processing software, including generation of reor maneuver commands). This was all controlled by a custom web interface to allow operators and scientists to quickly query data, verify attitude solutions, and generate reor maneuvers.

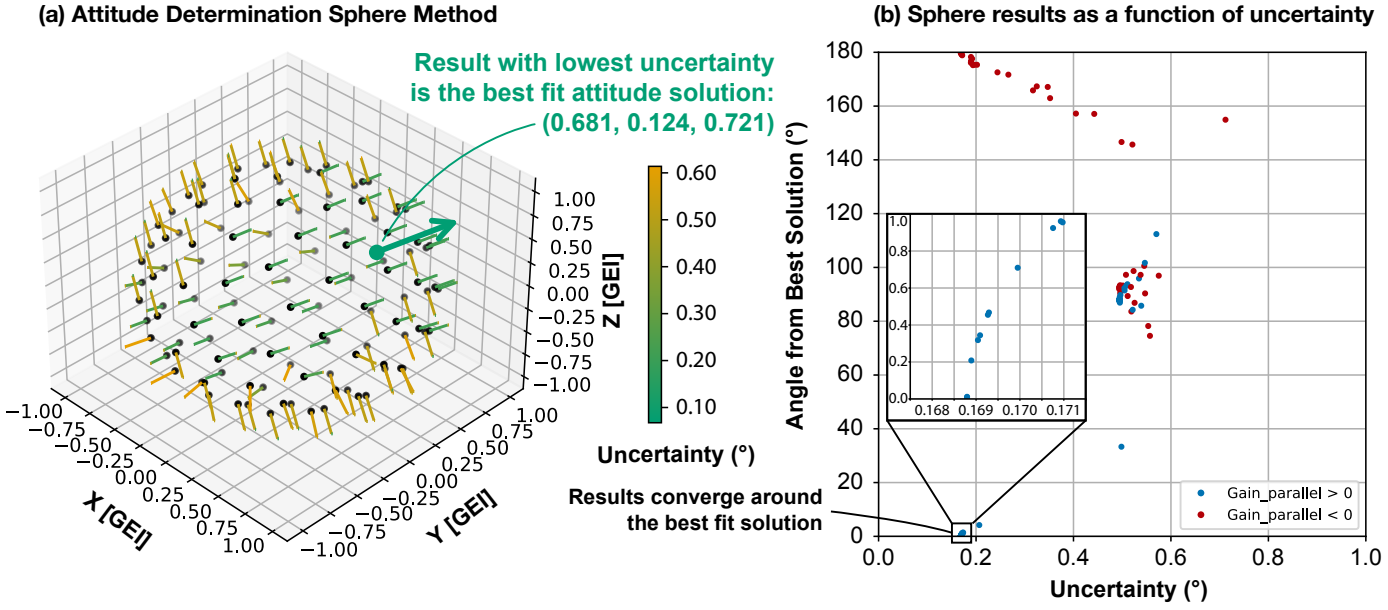

Fig. 8. Sphere solutions use many points evenly distributed on a unit sphere as initial attitude guesses for the fitting process. (a) depicts a 120-point sphere run using the data shown in Figure 7. The lines indicate the solution it converges to, based on the initial point (grayscale dot with shading representing distance to the viewer). The line color indicates uncertainty (higher uncertainty is orange). The green dot and green arrow show the initial guess and the solution with the lowest uncertainty; this is the final attitude solution that is used as "ground truth". (b) shows the angular difference to the best solution in the sphere as a function of uncertainty angular uncertainty. A inlaid zoom shows the stability of this method, since many points converge to within within a degree of the best fit attitude .

To obtain the attitude, we first provide a seed attitude vector S (i.e., a guess vector), which is typically the last known attitude. Next, we solve $B_{\parallel} = B_{igrf,gei} \cdot S$ for the spin axis component of the magnetic field $B_{z,ssl}$. Then, through a moving boxcar window, we solve (using minimum variance) for $B_{\parallel}$ and $B_{\perp} = B - B_{\parallel}$ components relative to the spin axis, which allows us to produce offsets and relative gains (because ELFIN is spinning stably about its Z axis). We then use the Levenberg-Marquardt (LM) multi-parameter fit (a damped least squares method) to numerically obtain the best fit to IGRF with the following parameters: $\text{Gain}_{\perp}$, $\text{Offset}_{\perp}$, $\text{Gain}_{\parallel}$, and spin axis angles θ and ϕ (all in body coordinates). The attitude is represented by the last two parameters, θ and ϕ, which describe the best fit spin axis that results in the best match between ELFIN's MRM data and the IGRF field. To confirm the validity of the attitude solution, we can plot the despun and calibrated MRM data on top of the IGRF field, shown in Figure 7 (top panel shows raw data, bottom panel shows fitted data). From this, we can simply estimate the error in the residual by taking its standard deviation about the mean in nT, or estimate the angular error by taking the geometric mean of the error about the mean, and the error of the mean compared to the IGRF model. With this method, we find angular errors typically well below $< 0.5°$. For a spin-stable spacecraft, there are only two attitude solutions that provide a good despun fit to the IGRF field: a solution close to the actual attitude vector and its opposite (with a negative gain, deemed unphysical). These two solutions correspond to global minimums in the manifold that describes this model within the parameter space, so if the guess vector is far away from either

solution, the algorithm may converge to a local minimum that is unstable (i.e., has large angular error). Therefore, if we need to ascertain the validity of an attitude solution output, we first look at the angular uncertainty to determine the solution trustworthiness, then validate with solar panel currents to ensure the sign is correct. Additionally, we can repeat this process across an entire sphere of initial guess vectors. This is shown in Figure 8a with the grayscale dots representing 120 seed vectors evenly distributed around the sphere (the shading denotes distance to the viewer, black is closer, gray is further away). The green arrow denotes the solution with the lowest uncertainty, and the rest of the lines lines point in the direction that the solution using that particular seed vector converged to. The color scale denotes the angular uncertainty with orange representing larger uncertainty; note that the green lines are thus either pointing along or opposite to the best fit solution. It is evident how sensitive the final solution is to the initial guess: for those points in roughly the same direction (around $\sim 30°$), all the solutions converge to the best fit solution. However, if the seed vector is too far off, the results can converge either in the opposite direction, a perpendicular direction, or somewhere in between with significantly more variance. The reliable sphere attitude determination method was used to establish ELFIN's "ground truth" attitude. We would then use an attitude propagation simulation, detailed in the next section, to model ELFIN's attitude in between solutions which would then be used for EPD calibration routines.

5.2. Attitude Modeling and Reorientations

At an inclination of about $\sim 93°$, ELFIN's attitude must keep up with the precession of its orbital plane as it rotates $\sim 0.5°$/day. In addition, the attitude control system must account for magnetic perturbation torques despite our best efforts to keep the spacecraft magnetically clean. This is due to the residual magnetic moment dipole from the batteries' steel casings and the shielded 2.5 kG octupole broom magnet in the EPDI instrument. The two battery pairs were placed inverted from each other on the -X side such that their moments would cancel; on the +X side, the EPDI's broom magnet was placed such that its dipole moment would be balanced by the batteries, minimizing the overall effective dipole moment. Ground testing in a magnetically clean chamber estimated the flight units to have nearly identical effective dipole moments in the range of $\mu_z = -0.015 \pm 0.005$ A m^2, consistent with our observations from spin-axis drift rate in Earth's field, in space. We care only about the magnetic moments along the spin axis because torques associated with the permanent magnetic moments on the spin plane $\mu_{x/y}$ are averaged out over the spacecraft spin.

On orbit, these perturbation torques amounted to a drift of up to $2°$ per day. Attitude modeling and reorientation maneuver generation is implemented in the Julia language (Bezanson et al., 2017), and a block diagram of its design is shown in Figure 9. The largest contributor to attitude drift was found to be the residual dipole moment and using a value of $\mu_z = -0.014 \pm 0.005$ and $\mu_z = -0.0125 \pm 0.005$ on ELFIN A and ELFIN B, respectively, was experimentally found to most closely fit ELFIN's spin axis on-orbit evolution over time. Figure 10 shows attitude modeling results (lines) filling in the gaps between actual solutions (dots) for ELFIN B over a 1 month period with no reors. The solutions generally converge well from one solution to the next. Average angular error for solutions one day apart was about $0.8°$, while accumulated angular error was up to $2°$ when modeling over a 7-day period. This indicates that the modeling stability is quite good, with low accumulated error. This is evident when examining the Z values of the spin axis in Figure 10, where it often seems like the attitude determination algorithm has converged on a spin axis Z value that is slightly off, despite having low statistical uncertainty. This remained an unresolved issue with our attitude determination algorithm, but was manageable given that the overall error still remained $< 1°$ even in the worst case scenario. Investigation of this issue is on-going, as an academic curiosity.

Figure 11 shows six months of attitude data from ELFIN-A from January 1 to June 1, 2022. In the top panel, the dots represent each of ELFIN A's attitude solutions (spin axis) in GEI coordinates connected by straight lines. The target attitude, the orbit normal

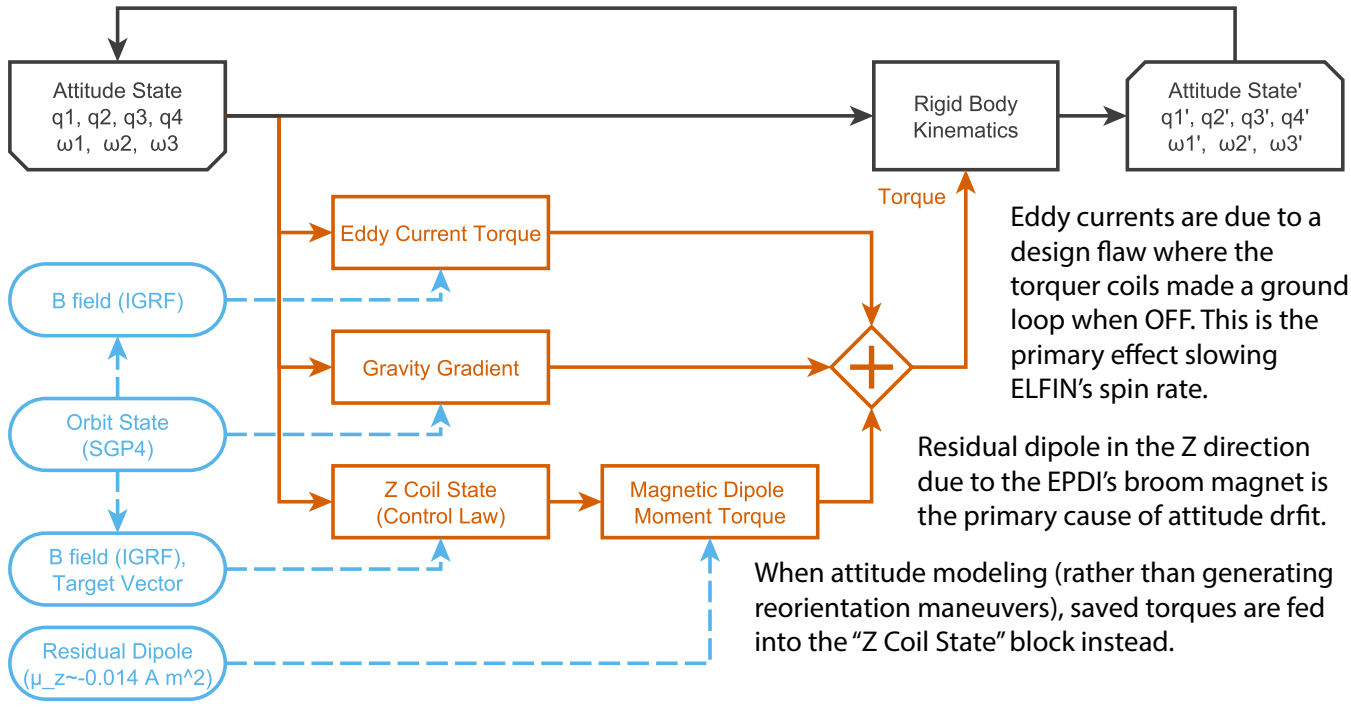

Fig. 9. Block diagram of the integrator used to model ELFIN's attitude, either to generate reorientation maneuvers operationally, or to model ELFIN's attitude between solutions.

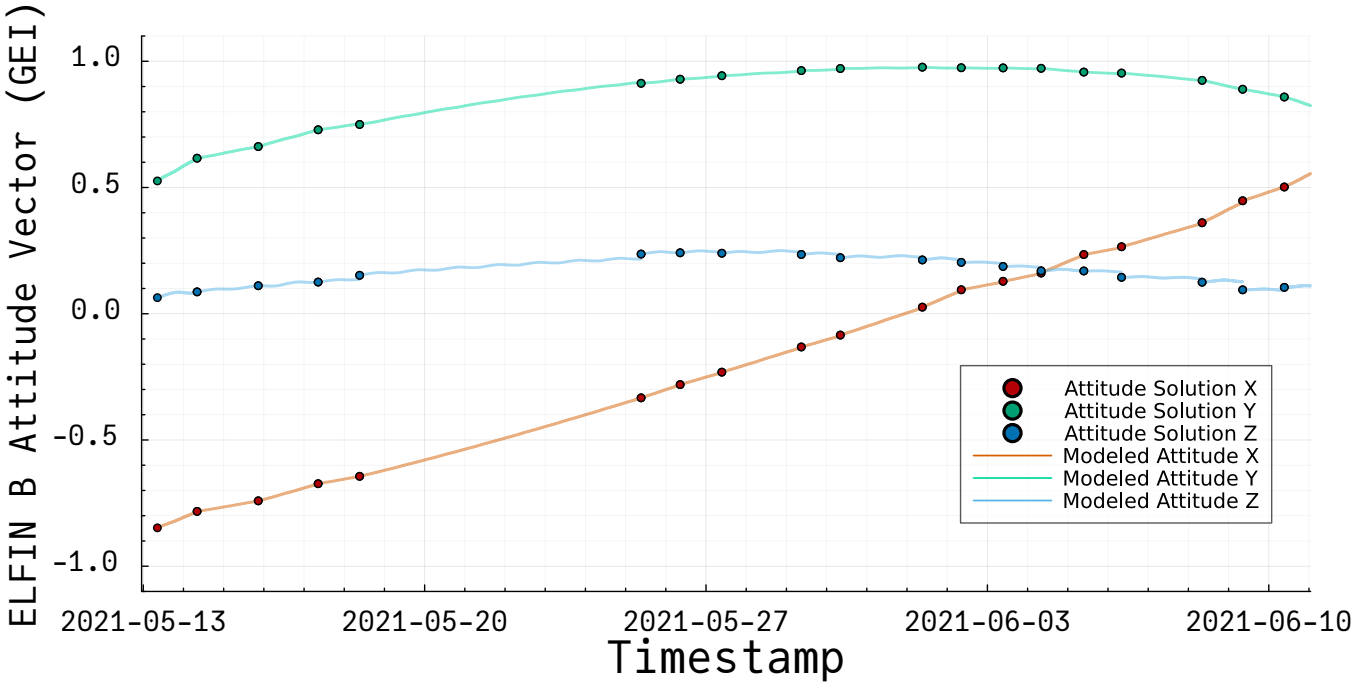

Fig. 10. Attitude solutions (assume ground truth) is shown as dots, while attitude modeling is used to predict ELFIN's attitude between solutions. Modeling works well even over long periods of time with no attitude solutions, but has some convergence issues in the Z_{GEI} axis(although the total angular error is trivial).

vector, is shown with the dashed lines in corresponding colors. Vertical dashed lines indicate each time a reorientation maneuver was performed, roughly once a week. In early April, ELFIN's orbital plane was approaching a noon-midnight orbit (for both spacecraft), which represents its worst power state with maximum shadow and less incident sunlight on solar cells. ELFIN A's

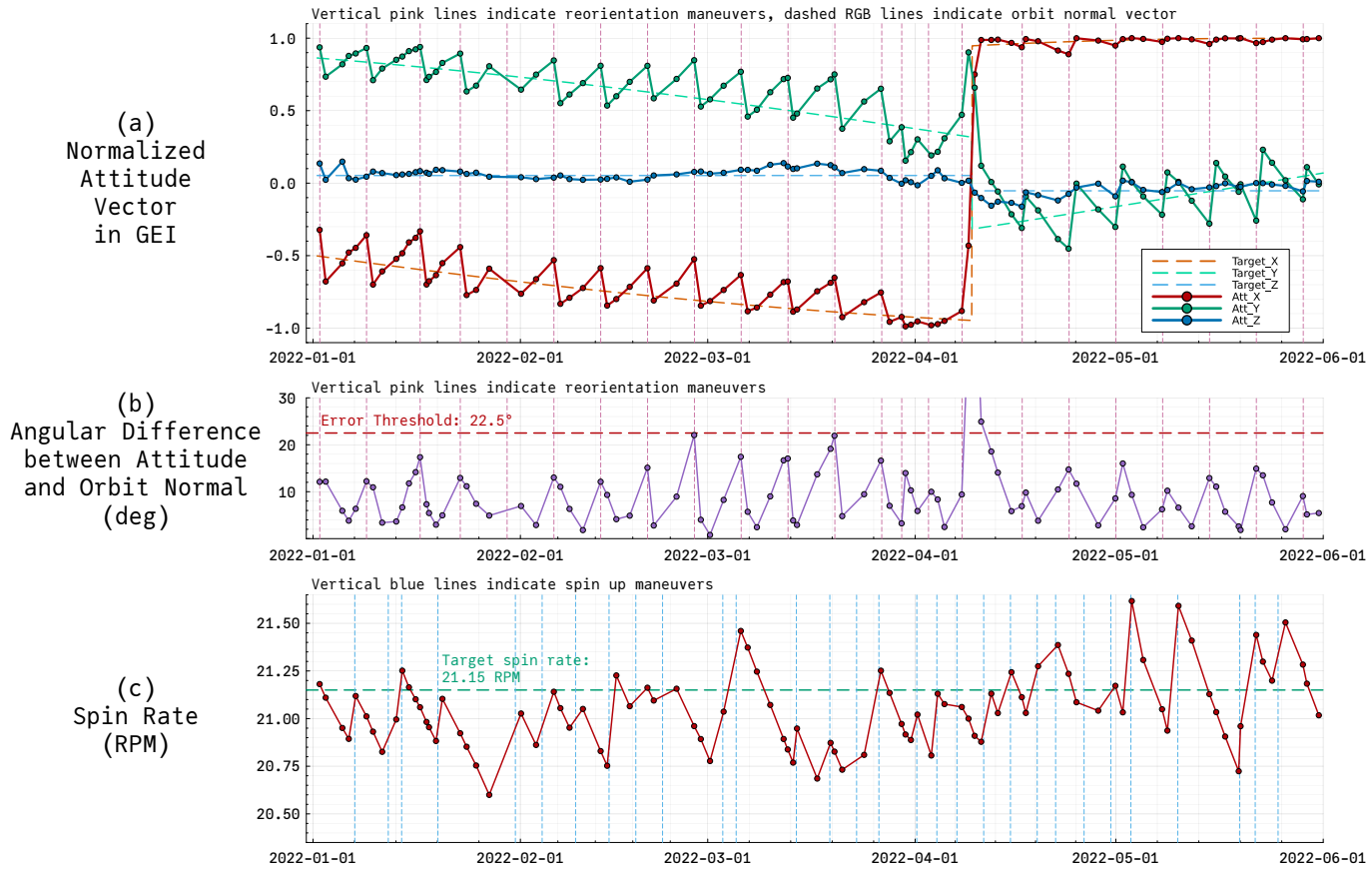

Fig. 11. This figure shows 6 months of ELFIN's attitude data from January 2022 to June 2022. (a) shows the attitude solutions in GEI coordinates with the target attitude vector in dashed lines. Vertical lines indicate reor maneuvers in both (a) and (b), keeping ELFIN's spin plane aligned with the orbit plane. On April 10th, 2022, a near-180° flip was performed in order to place the side of ELFIN that has more solar cells towards the sun for increased power input. (b) indicates the absolute angular difference between the target vector and ELFIN's attitude, where the science requirement is to keep the angle below 22.5°. (c) shows spin rate evolution over time with vertical lines indicating spin maneuvers.

attitude was such that, post noon-midnight, the -Z panel (with only 4 solar cells as opposed to the 6 solar cells on the +Z panel) would be facing the sun. Therefore, the team executed a ~ 155 degree flip, performing torques over 24 hours to rotate the spacecraft to a more optimal power state. Figure 11b shows the absolute angle between the attitude solution and the orbit normal vector, and during this flip, the target goal was to undershoot by 25 degrees for a more favorable power state (to satisfy science attitude requirements while maximizing power generation) while the natural attitude drift would slowly drift to the target vector as the orbit precessed. Even with such a large reor maneuver, the final attitude was only 1.92° off from the expected attitude. Typical reor maneuvers were generally around ~ 10 orbits long (~ 15 – 16 hours) and precise to within a degree of their intended target. Figure 11b shows that the operations team was able to reliably keep the spin plane aligned below the 22.5° threshold for optimal pitch-angle resolution, per mission requirements. Figure 11c shows spin control over time, keeping as close to the target of 21.15 RPM as possible. More details on spin control can be found in Appendix B.

6. Pitch-Angle Resolved Electron Distributions at LEO

Obtaining full pitch-angle distributions is important when trying to understand the coupling between magnetospheric, ionospheric, and atmospheric physics. For example, Capannolo et al., (2024) (to be submitted, paper title: "Unraveling the Atmospheric Energy Input and Ionization due to EMIC-Driven Electron Precipitation from ELFIN's Observations") used ELFIN observations

to examine the pitch-angle evolution of relativistic electron fluxes driven by EMIC waves. These energy-binned pitch-angle distributions provided previously unavailable inputs for the Boulder Electron Radiation to Ionization (BERI) model—a comprehensive ionization model (Xu et al., 2020)—and show that EMIC-driven precipitation contributes significantly to the production of ionospheric ionization and atmospheric ozone depletion. In addition, the backscatter of these electrons (i.e., electrons in the loss cone that bounce back and remain trapped for another bounce period) depends critically on their pitch-angle. Fluxes that are closest to the loss-cone are backscattered most efficiently, whereas electrons that are very field-aligned backscatter very little. This is why studies like Berland et al. (2023) use ELFIN's pitch-angle coverage within the loss cone to test their ionization models (see Figure 15 in Berland et al., 2023).

Another application of narrow FOV pitch-angle sectors cleanly sampling the loss cone is for the detection of microbursts, short-lived and intense bursts of electron precipitation that can reach MeV energies but typically last for $\sim$ 100 ms (Chen et al., 2022). Although not originally designed to study microbursts, ELFIN can identify them in the precipitation spectrum by sharp increases in the precipitating flux above ambient values anywhere within the loss cone when they become comparable to or exceed the trapped flux (see Figure 1b in Zhang et al. (2022a)). These ephemeral flux increases can only be differentiated from the trapped fluxes within a background of diffusive precipitation flux at least one order of magnitude below the trapped flux. This is only possible if precipitating fluxes are cleanly measured for multiple spin sectors within the loss cone (i.e., well-separated from the trapped fluxes) which can only occur when there is at least 45° between the loss cone edge ($\alpha_{LC} \approx 65 - 70°$ pitch-angle) and the detectors once per spin. This translates to an attitude requirement such that the B-field must be no more than $\sim 67.5° - 45° = 22.5°$ away from ELFIN's spin plane. This cannot be done fortuitously and requires control. Throughout the ELFIN era, $\sim$ 1000 microbursts have been identified (statistical analysis has been performed on 322 of those in Zhang et al., 2022a).

Indeed, nearly any scattering mechanism that drives energetic electron precipitation can be remotely studied using the ELFIN-measured precipitating-to-trapped flux ratio as a diagnostic. This ratio reflects the strength of the precipitation relative to its locally mirroring population as a function of energy and usually bears unique signatures of electron precipitation drivers; however, it can only be reliably measured with the correct spacecraft attitude. By aligning ELFIN's spin plane approximately with the orbital plane (since ELFIN is in a polar orbit), the full pitch-angle distribution can be resolved, and each population—trapped, precipitating, and backscattered—provides even more insight into precipitation drivers. In some cases, though, relying on the J_{prec}/J_{trap} flux ratio is not enough. For example, ELFIN data was used in Shen et al. (2022b, 2023b) to investigate electron losses driven by kinetic Alfven waves during substorm injections. The pitch-angle distributions were essential for distinguishing between anisotropic precipitation ($J_{prec} < J_{trap}$) driven by KAWs at low energies and whistler-mode waves at intermediate energies from isotropic precipitation ($J_{prec} \approx J_{trap}$) produced by field-line scattering at higher energies (see Figure 2(c-e) in Shen et al., 2022b). Hence, the use of both the J_{prec}/J_{trap} flux ratio and pitch-angle distributions together enable us to clearly distinguish between various precipitation drivers. These are therefore powerful remote diagnostics for studying magnetospheric phenomena.

Here, we show multiple cases of both J_{prec}/J_{trap} flux ratios and pitch-angle distributions from ELFIN that exemplify various types of wave-particle interactions or field line scattering in Figure 12. For each case, the energy spectrogram of trapped fluxes (locally trapped/outside of the bounce loss cone; top left panel), energy spectrogram of precipitating-to-trapped flux ratios (bottom left panel), and pitch-angle distributions (right panel) are shown. For example, EMIC wave-driven electron precipitation is characterized by intense MeV-level precipitation, and specifically exhibits a filled loss cone at MeV energies, but not at lower energies (as seen in Figure 12d and Angelopoulos et al., 2023; Capannolo et al., 2023). Whistler-mode chorus waves, on the other hand, are more effective at scattering electrons in the tens to hundreds of keV (Nishimura et al., 2010; Kasahara et al., 2018; Thorne

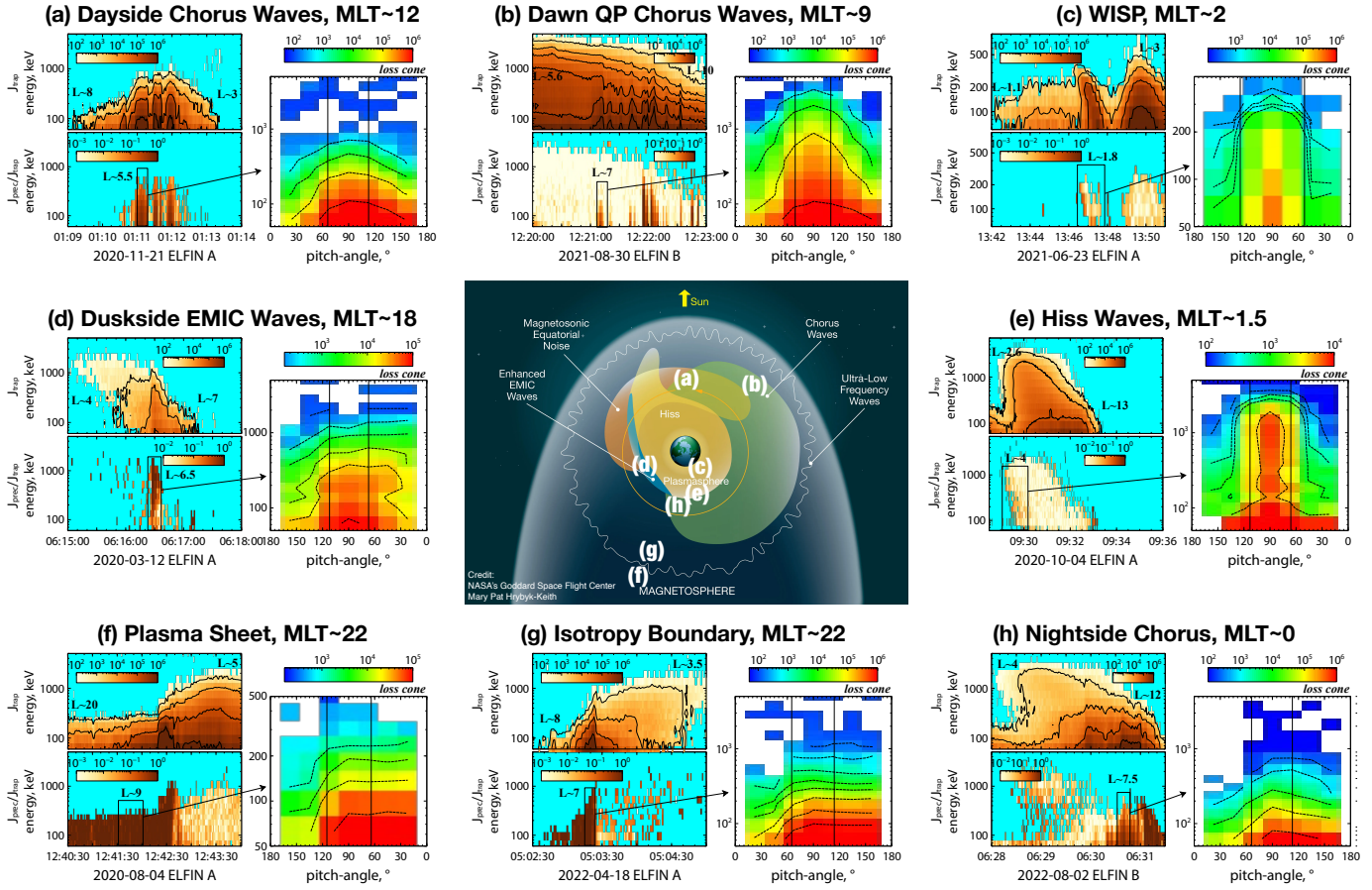

Fig. 12. Trapped electron flux energy spectrograms, electron precipitating-to-trapped flux ratio energy spectrograms, and pitch-angle distributions are shown for eight examples of wave-particle interactions (a-e, h) and field-line curvature scattering (f,g). Their typical locations are roughly mapped to their equatorial footprints in the magnetosphere, depicted with various wave populations and their locations (center image courtesy of NASA GSFC/Mary Pat Hrybyk-Keith)

et al., 2010; Ni et al., 2016; Nishimura et al., 2020). In particular, night-side chorus waves are typically quite intense and more field-aligned, resulting in rapid filling of the loss cone at the low hundreds of keV (as seen in Figure 12h and Tsai et al., 2024); however, waves on the dayside become oblique, resulting in a more diffusive-like process involving high-order resonances where precipitation is more intense closer to the loss cone edge and weaker further away (as seen in Figure 12a and Gan et al., 2023). WISP precipitation, driven by VLF transmitters, is very diffusive and characterized primarily by its energy dispersion as a function of L-shell (as seen in Figure 12c and Shen et al., 2022a). Electron precipitation in the plasma sheet and isotropy boundaries are isotropic and are represented by loss cones filled at all energies above the curvature scattering threshold (as seen in Figure 12(f,g) and Artemyev et al., 2022a; Wilkins et al., 2023). In the plasmasphere, whistler-mode hiss waves are effective in weak but persistent scattering of sub-relativistic electrons, providing weak flux levels within the loss-cone and depleting trapped fluxes at low altitudes (as seen in Figure 12(e) and Mourenas et al., 2021).

7. Discussion

7.1. Lessons Learned

The ELFIN mission, despite being UCLA's first CubeSat mission, has returned an unprecedented amount of science and, by some metrics, compares favorably against other space weather missions. As of this writing, ELFIN's "peer-reviewed publications (PRP) per years-since-launch (YSL)" is 7.9 (see Table 1 in Spence et al., 2022)—more than double any other space weather CubeSat.

ELFIN achieved this while also being entirely-student run, with undergraduate students in leadership positions driving system architecture and engineering design decisions. The ELFIN mission therefore makes an outsized educational impact, having given around 350 students the ownership and responsibility typically bestowed upon those much further along in their careers. On average, students typically join the team for 3 years, which gives more senior undergraduates plenty of time to transfer knowledge to the more junior ones. Continuity of knowledge is additionally maintained through well-organized documentation and staff mentorship. This prepares students for the future while simultaneously preparing the institution for future CubeSat-based science investigations.

Despite the promises of high science output by small, low-cost satellites, university-class CubeSat missions still seem to be struggling to gain their footing in NASA's portfolio. Only 10% of CubeSats successfully completed their missions and at least 77% failed before full mission completion for all university-class CubeSat missions from 1970-2018 (the 2018-2023 numbers do not appreciably improve, see Figures 10-14 in Swartwout, 2023). Indeed, there were many points along ELFIN's development and operations timeline where achieving full mission success did not seem feasible. Several of these occurred during integration and test, but the majority occurred during post-launch operations. Accordingly, we briefly highlight five important factors contributing to ELFIN's success; the first one is commonly repeated in this field, but the rest apply specifically to post-launch operations covered in this paper.

- *Functional hardware and rigorous system-level testing:* This is the minimum requirement to make it past the infant mortality threshold where so many CubeSat missions end. ELFIN's schedule was facilitated by a fortuitous 1-year launch delay of the prime mission which gave our team the necessary time to complete a full range of system-level tests. These included representative range tests, component and system-level thermal vacuum cycles, and thorough instrument calibration. As a result, ELFIN had no major hardware issues on orbit, allowing the team to focus on resolving operational challenges.

- *Process-driven priorities:* Due to a lack of student experience, the ELFIN team had focused too much on getting as much data as possible in the beginning of the mission. The team was motivated by scientific results, but had no pre-planned means to achieve long-term high-yield data throughput. The early declaration of mission success from the first storm data acquired allowed the team to take a step back and reconsider its operations paradigm. By shifting the focus away from brute-force data collections towards fixing the processes and underlying software tools that can enable efficient operations, the team was able to use its operations experiences to build a sustainable, future-proof, and scalable satellite operations paradigm that quickly produced results. Good processes are tailored to each individual mission and flight architecture, and, for newer teams, as was the case here, such processes were in fact easier to determine once in orbit.

- *Post-launch development time:* In orbit, the team deliberately tackled problems one at a time according to science priorities: first calibrate electron data (primary science); then fix operational issues and ADCS; then calibrate ion and FGM data (secondary/tertiary science). Resolving each of these problems involved an interdisciplinary team of scientists, operators, and software developers that worked closely together for months, and the end result was not just a successful mission, but an operations-hardened team with a wealth of situation-specific knowledge ready for the next challenges in their careers, including, for some, their next CubeSat mission. In a sense, this is the most effective type of capacity building. A lesson learned, therefore, is that teams should plan to have adequate funding, schedule, and personnel dedicated to post-launch development work.

- *Infrastructure and motivation:* Students are eager to work on something destined for space because there is a clear goal with concrete work to be done. However, we found that students were less interested in operating something that was

already in space, and the team attrition peaked shortly after launch, further straining the mission. Since ELFIN's entire operational pipeline was designed and built at UCLA, the motivation was shifted to focus on ownership of the ground support infrastructure, including but not limited to operations software, ground stations, management tools, and internal development tools. We found that the students really enjoyed this because it taught them valuable industry skills that they were unlikely to find even in industry internships. This created a positive feedback loop between developing optimized infrastructure for ELFIN and daily satellite operations. This had many benefits beyond giving students ownership of something tangible, since it boosted team efficiency and played a big role in sustainable capacity building at the host institution for future missions.

- *Open-access data and analysis tools:* After nearly three years of hard work focusing on data calibration and building automated data processing pipelines, we were confident enough to release data publicly in July 2021. In addition to hosting ELFIN data on public NASA Space Physics Data Facility (SPDF) and UCLA servers, we also maintained data analysis tools (via a SPEDAS plugin) for scientists to analyze ELFIN data in the greater context of the Heliophysics System Observatory (HSO). In addition, online quick-look summary plots were publicly available, allowing anyone to view the latest calibrated ELFIN data contextualized by geomagnetic indices, ground station coverage, spacecraft conjunctions, and more, all within an hour of data being downlinked. Assisted further by Autohban reports (mentioned in Section 4), any operational or scientific issues were quickly resolved. Summary plots are available here (`https://plots.elfin.ucla.edu/summary.php`), data retrieval of individual files is here:(`https://data.elfin.ucla.edu`), and access to the latest version of SPEDAS is here: (`https://spedas.org/wiki/index.php`) (see Angelopoulos et al., 2019).

These lessons are most applicable to student-run missions like ELFIN, where students own the mission end-to-end. For example, students learn to construct and maintain a thermal vacuum chamber, build roof-mounted satellite antenna towers, build and maintain custom DevOps infrastructure, build and test cutting-edge scientific plasma instrumentation, and even calibrate these instruments on-orbit while being responsible for daily communication with two satellites. These are powerful problem-solving experiences that provide students with real-world, hands-on research and satellite technology development experience in an accessible and cost-effective manner. We believe that this is the best way to do capacity building: with a focused science mission and a vertically integrated team that aligns scientists, engineers, and students toward a common goal. Through several generations of students, we have built up a skilled and supportive network of alums in industry and federal agencies who are willing to review, mentor, and even collaborate. This not only reduces future technical risk, but also reduces the barriers to entry for the typically-stringent fields of aerospace and heliophysics, further incentivizing students from diverse backgrounds to participate. At a fraction of the cost of larger missions, ELFIN has impressed rigorous industry and academic skills upon hundreds of students while conducting a wide-range of compelling space research and developing institutional knowledge and credibility for future flight opportunities.

7.2. Value of Electron Precipitation Data Sets

ELFIN, with its unique perspective within the entire pitch-angle range (including resolution inside the loss-cone), provides scientists with fresh insights into magnetospheric processes from the inner radiation belt, through the plasmasphere, and all the way into the plasma sheet. So far, ELFIN's long-term monitoring (over three years) of energetic electron precipitation and locally trapped fluxes has provided an extensive dataset that will continue to be the basis of many scientific investigations. In fact, several studies have already shown the complementary value electron precipitation data sets provide when paired with a variety of different instruments. For example, Shen et al. (2022b) and Artemyev et al. (2024b) have demonstrated the use of simultaneous energetic and thermal ($1 - 30$ keV) electron populations using conjunctions with MMS and DMSP, opening key questions regarding the

energy input of substorms in the ionosphere and the origins of sub-auroral polarization streams (SAPS). Zhang et al. (2023b) also demonstrated the use of GPS-provided total electron content (TEC) in conjunction with electron precipitation for probing ionospheric density structures and drift behavior. High-resolution magnetic field measurements have been used to localize energetic electron precipitation relative to the primary magnetosphere-ionosphere current systems (Shen et al., 2023a,b). These studies reveal the value of contextualized electron precipitation measurements and demonstrate that a future ELFIN-like mission would be invaluable towards advancing the predictability of space weather.

Additionally, increasing the time and energy resolution of energetic electron measurements is principally important for studying the most intense short-scale precipitation events (Zhang et al., 2022a,b). Phenomena at these timescales are associated with waves, so combining future electron precipitation measurements with wave measurements—for example, a high-resolution DC magnetometer for EMIC waves and an AC magnetometer for whistler-mode waves—would vastly expand our understanding of the mechanisms behind wave-driven electron scattering.

Although ELFIN has already deorbitted, we may not have to wait long for the next in-situ particle precipitation measurements: the Relativistic Electron Atmospheric Loss (REAL) CubeSat mission (Millan et al., 2018) has this capability and is slated for a March 2024 launch. REAL is 3-axis stabilized with multiple look directions and an energy range with a lower energy floor and should yield significantly higher time resolution captures of electron precipitation compared to ELFIN. A similar instrument is expected to fly on CINEMA (NASA SMEX mission currently in phase A) as well, and draws upon the same benefits of a 3-axis stabilized spacecraft. However, spinning satellites like ELFIN are still necessary because they can measure precipitating, trapped, and backscattered electrons (i.e., full 360° pitch-angle distribution) with the same detector. In addition to the applications covered in Section 6, this is important because inter-calibration between multiple detectors/look directions that do not see the same fluxes is more difficult to validate. Higher time and angular resolution can be achieved by adding more detectors in the spin plane (inter-calibration this way is far easier because the different detectors will measure the same fluxes as a function of pitch-angle during stable quiet periods) and increasing the angular sectors per spin. The feasibility of sampling at 32 sectors rather than 16 was demonstrated on ELFIN briefly via a software update (one week of data per spacecraft was indeed collected at the higher sector rate), but it was deemed unwarranted in the long-run, given the doubling in EPDE data volume it entailed, compared to the value of ion collections, inner belt collections and additional SZ collections that would otherwise be sacrificed.

Together with other spacecraft and ground-based measurements, ELFIN has played a crucial role in advancing our understanding of space weather. The novel electron precipitation data sets have revealed fresh insights in (and continue to remain valuable for) investigating magnetospheric-ionospheric coupling and wave-particle physics. For just over four years, the ELFIN student team successfully communicated with both ELFIN satellites on a daily basis: this experience has demonstrated that a well-suited operational approach leads to efficient and sustainable daily operations, facilitating successful, enduring scientific missions with low cost and high science return. The aforementioned technical innovations resulted in novel electron precipitation data sets which have revealed a multitude of new insights and continue to be useful in the study of magnetospheric-ionospheric coupling and wave-particle physics.

Acknowledgments

We acknowledge support by NASA awards NNX14AN68G, 80NSSC23K1038, 80NSSC23K0108, 80NSSC19K0844, and 80NSSC22K1005, along with NSF grants AGS-1242918, AGS-2019950, and AGS-2021749. We are grateful to NASA's CubeSat Launch Initiative and Launch Services Program for ELFIN's successful launch in the desired orbits. We acknowledge early support

of ELFIN by the AFOSR, under its University Nanosat Program, UNP-8 project, contract FA9453-12-D-0285, and by the California Space Grant program for student support during the project's inception. Importantly, we acknowledge the critical contributions and sacrifices made by several hundreds of UCLA students; many rose to the challenge at just the right time, and it is the sum of all those years of effort that made ELFIN a success. Furthermore, ELFIN downlink support was generously provided by StellarStation (`https://www.stellarstation.com/`), NASA Wallops, Montana State University (Keiji Yoshimura, Arlo Johnson, Tyler Holliday), and numerous amateur radio listeners from all over the world `https://satnogs.org/`. Finally, we are grateful for the advice and generous time contributions from our post-delivery reviewers, unofficial mentors, and our biggest supporters: Aerospace Corporation: Garrett Kinum, David Hinkley, and Bernie Blake; Apple: Pat Cruce; Terran Orbital: Chris Shaffer; and Cal State University Northridge: James Flynn.

Appendix A. Refactor 2.0 Concepts and Rules

Appendix A.1. Key Concepts

Intents and Allocations are defined in the main text and serve as neatly organized abstractions that are human-readable, state-trackable, and flexible enough to accomplish all nominal and off-nominal in-flight tasks required of ELFIN. These intents and allocations are created by the operator in the Planner software, but there is still the process of turning them into commands, sending them to the spacecraft, and verifying each step along the way.

As shown in Figure A.13, once Allocations are created within the Planner, they are translated into commands via the **Translator**—a software module within the Planner—and exported to the database. Operators can then use the **Commander** to convert the translated output into a **Load File**. The Commander is a separate software module that manages both real-time commanding and Load Files: files that store series of commands and associate them with a specific pass. These Load Files are saved on the Main Server and can be executed autonomously even in the event of communication loss between the ground station and the Mission Operations Center.

With these abstractions in place, we now define the data and knowledge models that then allow for the specification of rules which govern Intents and Allocations. We first begin with the **Ground Truth Model**: an idealized representation of state assuming a perfect computer network with no risk of data loss. It splits the classification of Allocations into three categorizations:

- **Pending** refers to Allocations that do not yet exist aboard the spacecraft (i.e. they exist only in the Planner).
- **Live** refers to Allocations that have been written to the spacecraft and are therefore going to be executed.
- **Stale** refers to Allocations that that have been overwritten or are otherwise invalidated due to, for example, an elapsed timestamp.

However, our communications link is not perfectly reliable as it is possible to drop uplink or downlink packets in our communications, due to RF nulls from spinning. Further, our infrastructure within a primarily educational institution—rather than a primarily space mission facility—does not guarantee 100% uptime for both network access and power, meaning that our knowledge models must be resilient against failures in both uplink and downlink: we cannot always assume commands will successfully make it onto the spacecraft. In order to handle this, the Planner's state tracking relies on the **Planner Model**, which slightly expands upon the Ground Truth Model:

- **Pending** now refers to Allocations that have not yet been translated into a command (i.e. they are still within the Planner).

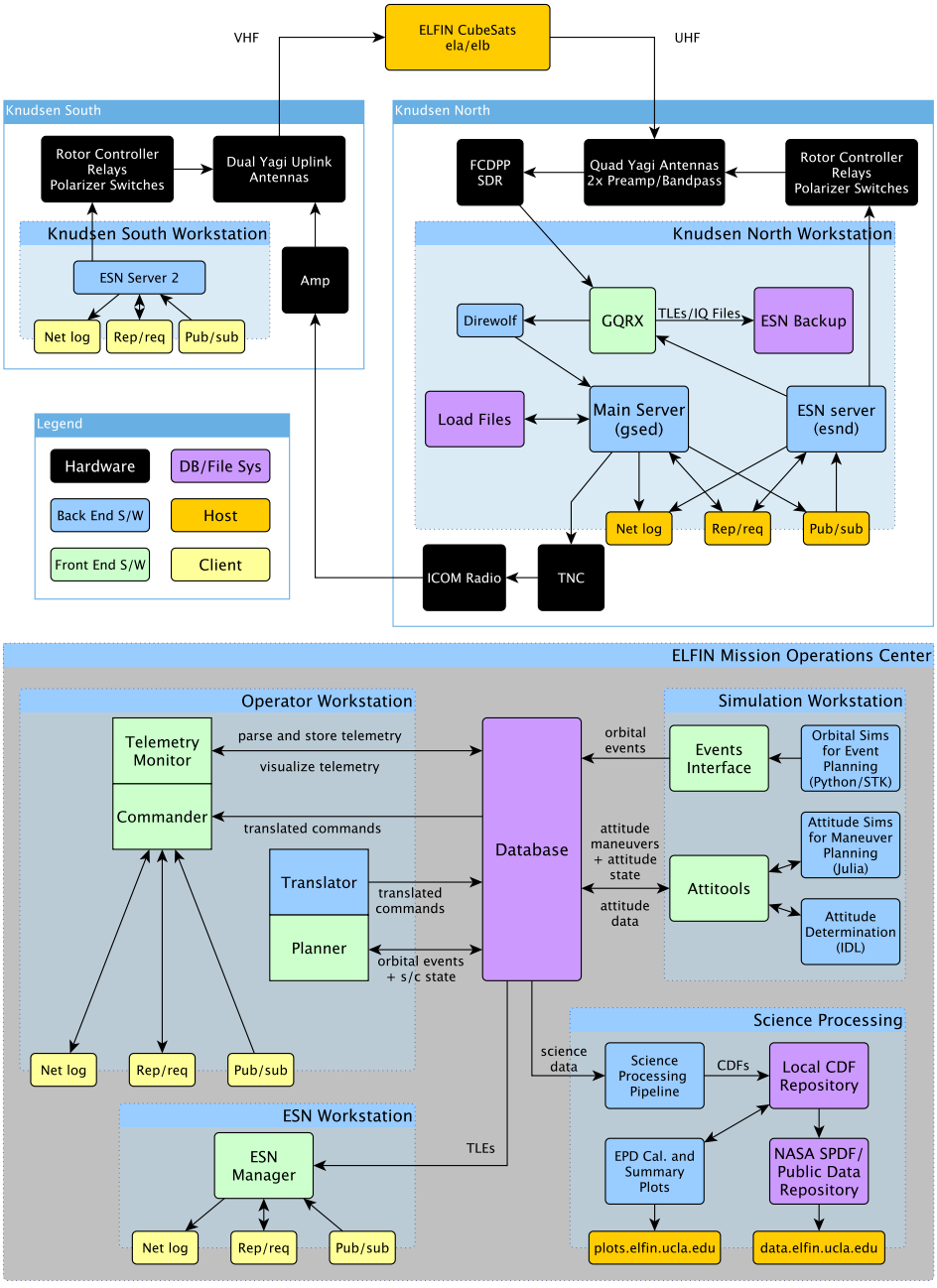

Fig. A.13. A block diagram of all ground software used to support ELFIN.

- **Translated** refers to Allocations that have been translated but not yet transmitted (i.e. they have left the Planner and are potentially in a Load File waiting to be uplinked during an upcoming pass).
- **Sent** refers to Allocations that have been sent to the spacecraft and may exist onboard, although they have not been verified yet.
- **Confirmed** refers to Allocations that have been verified to be written aboard the spacecraft.
- **Stale** refers to Allocations that have been overwritten by another “confirmed” Allocation or are otherwise invalidated by an elapsed timestamp.

Verifying commands is done by the Commander in real time upon sending/receiving each command. Each command contains both a write and read bundled into the same frame and contains both an associated Intent ID and associated Allocation ID. If the readback of the onboard Resources match expectations, the Allocations are marked Confirmed in real time. This is important because in special cases (e.g., overwriting or wiping a preexisting intent), it is desirable to only uplink commands if previous commands have been confirmed successful. An Intent state will reflect the weakest state of its Allocations, so that an Intent will only be confirmed if all Allocations within it are also confirmed. These states are color-coded in the Planner GUI (see Figure 6) at both the Intent level (for the overall summary view) and Allocation level (when using the wizard).

The **constraint checker** is the underlying software running within the Planner, that handles logic and adherence to Refactor 2.0 rules throughout all the wizards and planner actions. The states from the Planner Model are further grouped into ground truth states which are used for constraint checking:

- **Possibly live:** "sent" and confirmed".
- **Possibly stale:** "stale" and all but the most recent from "possibly live".
- **Future live:** "translated", "sent", and "confirmed".
- **Future stale:** "stale" and all but the most recent from "future live".

The logical flowchart shown in Figure A.14 shows how the constraint checker enforces these rules and acts as a backend module within the Planner which other modules can interface with.

Appendix A.2. Planner Rules

Leveraging the framework described above, the constraint checker can now enforce the two directives that govern safe operating:

1. Prevent any scheduling conflicts between activities.
2. Handle uncertainty in the safest and strictest way possible.

Prevent scheduling conflicts: Intents with overlapping scopes cannot coexist onboard the spacecraft. If a new Intent overlaps with any existing Intents, the new Intent must include all the resources for which the overlapping Intents have non-stale Allocations that are not wipes. This allows us to make the Intent Scope Assumption: if two Intents of the same type overlap, their scopes are identical. Additionally, new Intents may not interfere with any other already-scheduled activity and time-allocation rules must prevent overlap with all other non-stale Intents.

Handle uncertainty: Disallow overwriting active schedule entries and discourage situations in which a new Intent allocates a non-stale resource. If a new Intent allocates a non-stale resource, it must allocate all other non-stale resources which share the same Intent. We also enforce the ordering of Allocations such that any Allocation can only be replaced by a newer Allocation. Stale Allocations are no longer actionable, and an Allocation can only be translated or transmitted if it is not future stale. Because pending Intents have no explicit ordering when they exist within the planner, we enforce stricter rules for pending Allocations. Thus, a resource may not be re-allocated while there exists a pending Allocation that uses it, and an Intent may not be created if it overlaps with another pending Intent.

These lead to a few key assumptions. The In Order Assumption: Intents exist onboard the spacecraft in the same order in which they were allocated on the ground (FIFO), barring any Intents which were never successfully written. Only the latest translation output can be included in a load file, and if load files contain multiple translated Allocations for the same resource (i.e., overwriting

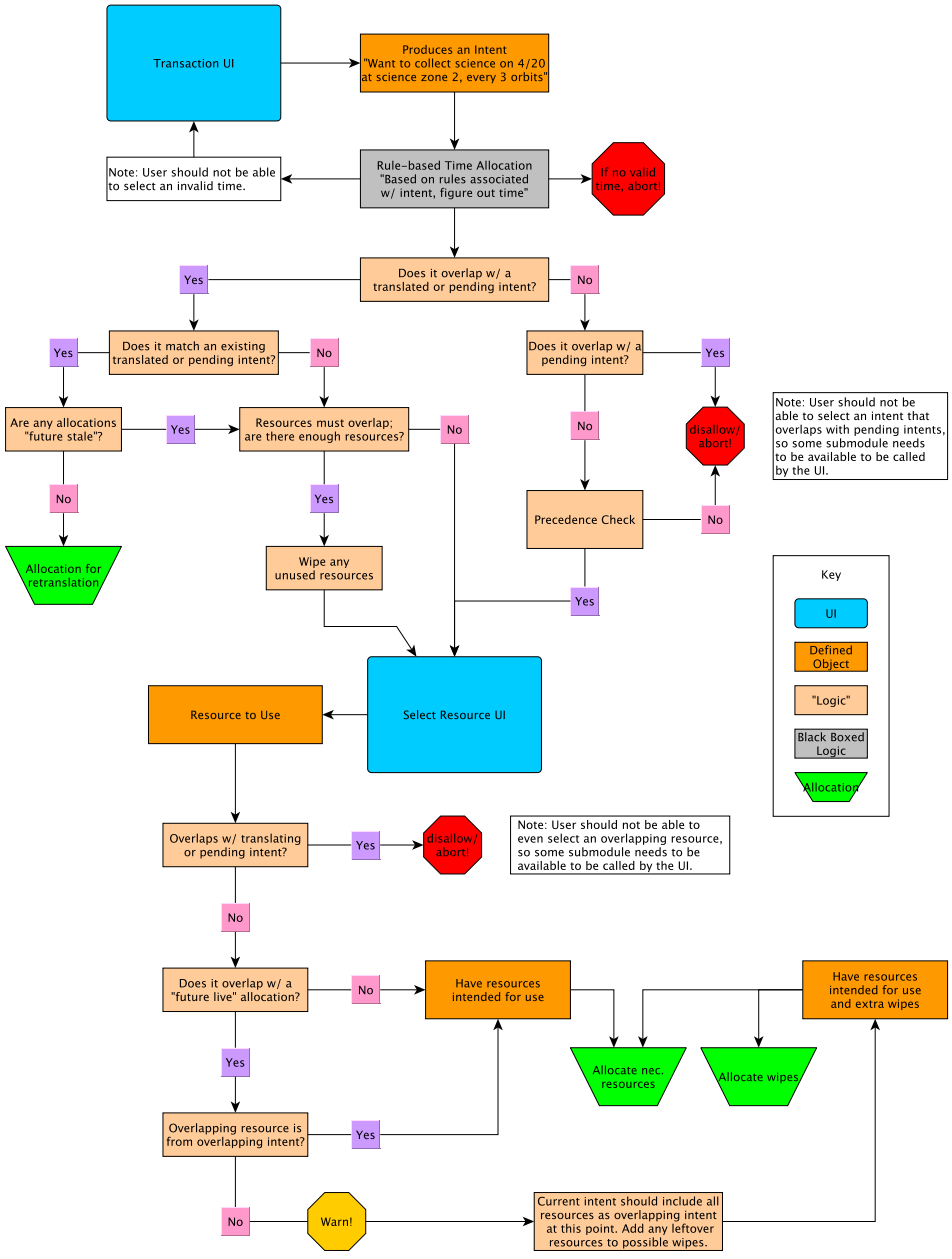

Fig. A.14. Logical flowchart demonstrating the type of decisions the constraint checker would make in order for operators to safely make Allocations.

of resources), the older Allocations only appear in load files earlier than any Allocations which are newer than it. This required upgrading the Commander to have real-time command verification and conditional commanding, opting not to send commands until its prerequisite commands are also verified to be onboard.

We can also make the atomicity assumptions: Allocations are atomic, and Intents are pseudo-atomic. Intents cannot be fully atomic—due to the byte-size limitation of AX.25 packets—and some Intents are too large to fit in a single radio packet. This requires Allocations to only be transmitted along with the rest of the Allocations in their respective Intent. The discrepancy between the atomicity of Intents and Allocations means special care must be taken to ensure that a mix of two Intents can never simultaneously exist (no "Frankenstein Intents"). If an Intent has too many Allocations to fit in a single uplink frame, the first frame includes a wipe of the entire resource, and the second frame is only transmitted after the wipe succeeds, relying on the conditional commanding framework alluded to in the previous section.

These rules served to provide structure to the complete operational freedom of the original design that allowed for too much uncertainty. Whenever an option presented itself, the Planner would delegate set choices to the operator in a safe manner, as dictated by the constraint checker, rather than giving the operator free reign. For example, the resource-picking step in each Intent creation wizard would present a list of all resources with color-coded statuses; the operator can then see all resources and deliberately pick resources rather than allowing software to automatically pick any free resource. There was still operational freedom, since the operator could pick a live conflicted resource if they so wished, but the constraint checker would force the selection of all other associated resources to preserve the atomicity rule. When generating commands, the Commander would automatically insert wipes as needed to ensure safe uplink of these Allocations. With thoughtful design, these choices were easy for the operator to make because we chose to keep the software transparent while avoiding hidden complexity and nondeterministic behavior.

Appendix B. ELFIN Spin Control

Appendix B.1. Spin Control

Ground determination of spin rate is determined by finding the power spectrum on the 24-minute snippet of MRM data and taking the peak frequency. This is what is used for science data and determining when operators need to schedule the spacecraft to spin up or down. Spin control is performed using one of two modes: B-act or B-dot.

B-act relies on waiting until the magnetic field is largest in the spacecraft body X direction; by turning the Y-coil on at that time, a torque can be generated in the Z direction to either spin the spacecraft up or down. This is a very simple algorithm that does not require onboard spin knowledge. The only complication with ELFIN's design is that turning on the Y-coil produces a strong B field in the Y direction, so measurements cannot be used when the coil is powered. To mitigate this, B-act can be configured to have variable duty cycle levels, where the coil remains on for a specified amount of time before turning off and waiting for a specified number of magnetometer samples (during control law, the magnetometer is sampled at 56.25 samples per second) before checking for the original B-act condition to be met again. Ground testing showed that the coil drivers were so fast that they could not be detected within one sample of turning off. Because B-act was designed to be used when ELFIN was first deployed and barely spinning, we began by torquing for 28 samples ($\sim$ 0.5 seconds) and turning off for 4 samples (an 88% duty cycle). Both ELFINs were brought to a target of 10 RPM before switching to B-dot.

B-dot uses a 7-point Finite Impulse Response (FIR) filter to take a digital derivative of the magnetic field, thus keeping the algorithm unaffected by the flat pulses of the torquer coils. To determine duration of torque, the attitude controller uses half-periods (periods between the zero crossings) of the Y-axis B-dot value. It then torques based on the sign of B-dot in the Y-axis. The duty

cycle here is also configurable, and was set to a default of 50% of the half period, meaning that the coils would turn on for a quarter of a spin centered around the middle of the zero crossings (i.e., centered on the maximum or minimum X values). The advantage of B-dot is that the coils do not have to turn off during the ideal torque phase and the total torque provided is symmetric, leading to marginally higher precision and efficiency.

There were a few additional safeguards implemented as a result of ground testing: spike detection and H_{lim}. H_{lim}, short for hysteresis limit, was implemented because the noise of the MRM (around 300 nT) meant that there were often consecutive zero crossings close to each other. An H_{lim} value prevents the detection of a new zero-crossing after n samples, which were often smaller than the current spin rate (default 10 samples, or about 178 ms). The other issue was that the MRM would sometime have random spikes in the data where a single isolated value would suddenly have a large offset. This was unnatural and occurred in only 1 axis at a time. The mitigation for this was to check the difference between each measurement n and $n-1$. If the delta exceeded a specified threshold, the value would be evaluated to be the average of $n-1$ and $n+1$. This resulted in all sampling having one sample (or 18 ms) lag. A bigger delay was the 7-point FIR filter used in B-dot, resulting in a filter delay of 3.5 samples (or 62 ms) and a total delay of 4.5 samples (80 ms). These delays were negligible at ELFIN's spin rate and the spin control worked nearly as intended on orbit.

The one major issue regarding ELFIN's spin paradigm was a design flaw associated with the torquer coil drivers. When the coil was in the OFF state, the coils were shorted to ground rather than left open. An eddy current would thus be generated in the spin plane (i.e., in the Y-coil) to oppose the field with strength equal to the time-derivative of the external field. Because the field is rotating, its derivative will cause an induced magnetic field rotating in the same direction (with the opposite sign), but its time-profile will have a 90° phase shift to the original field. The induced moment produces a torque along the spin axis (a despin) and a minor torque off-spin axis (depending on the alignment of B field and spin plane). The total torque imparted is given as follows:

$$\vec{\tau}_{\text{eddy}} = \vec{M}_y \times \vec{B} = \left(\sigma N^2 A^2 \mu_y\right) \hat{y} \times \vec{B} \tag{B.1}$$

where σ is the wire conductance, N is the number of turns in the Y-coil, A is the area of the Y-coil, θ is the angle between the Y-coil and the B field, and μ_y is the relative permeability of the spacecraft. Since the despin rate is fixed and measureable, we can compute the effective relative permeability of each satellite (with primary contributions from the steel-cased batteries and mu-metal magnetic shielding in the EPDI) which was experimentally found to be about $\mu_y = 18$. The rest of the values are known and can be applied to calculate the torque, which is then integrated over the orbit. The resulting equivalent moment comes out to be $O(10^{-4})$ Am^2 which is negligible compared to the residual dipole discussed earlier. However, the overall despin torque comes out to be $O(10^{-8})$ Nm which resulted in the 0.1 RPM/day loss observed on both ELFIN satellites. While this was larger than anticipated, scheduling 10 minute long spin-up maneuvers twice a week incurred only a trivial schedule and power cost and did not meaningfully impact nominal operations.

References

An, X., Artemyev, A., Angelopoulos, V. et al. (2022). Nonresonant Scattering of Relativistic Electrons by Electromagnetic Ion Cyclotron Waves in Earth's Radiation Belts. , *129*(13), 135101. doi:10.1103/PhysRevLett.129.135101.

Angelopoulos, V. (2008). The THEMIS Mission. , *141*, 5–34. doi:10.1007/s11214-008-9336-1.

Angelopoulos, V., Cruce, P., Drozdov, A. et al. (2019). The Space Physics Environment Data Analysis System (SPEDAS). , *215*, 9. doi:10.1007/s11214-018-0576-4.

Angelopoulos, V., Tsai, E., Bingley, L. et al. (2020). The ELFIN Mission. , *216*(5), 103. doi:10.1007/s11214-020-00721-7. arXiv:2006.07747.

Angelopoulos, V., Zhang, X.-J., Artemyev, A. V. et al. (2023). Energetic electron precipitation driven by electromagnetic ion cyclotron waves from ELFIN's low altitude perspective. *Space Science Reviews*, *219*(37). doi:10.1007/s11214-023-00984-w.

Artemyev, A. V., Angelopoulos, V., Zhang, X. J. et al. (2023). Dispersed Relativistic Electron Precipitation Patterns Between the Ion and Electron Isotropy Boundaries. *Journal of Geophysical Research (Space Physics)*, *128*(12), e2023JA032200. doi:10.1029/2023JA032200.

Artemyev, A. V., Angelopoulos, V., Zhang, X. J. et al. (2022a). Thinning of the Magnetotail Current Sheet Inferred From Low-Altitude Observations of Energetic Electrons. *Journal of Geophysical Research (Space Physics)*, *127*(10), e2022JA030705. doi:10.1029/2022JA030705.

Artemyev, A. V., Demekhov, A. G., Zhang, X. J. et al. (2021). Role of Ducting in Relativistic Electron Loss by Whistler-Mode Wave Scattering. *Journal of Geophysical Research (Space Physics)*, *126*(11), e29851. doi:10.1029/2021JA029851.

Artemyev, A. V., Zhang, X. J., Demekhov, A. G. et al. (2024a). Relativistic Electron Precipitation Driven by Mesoscale Transients, Inferred From Ground and Multi-Spacecraft Platforms. *Journal of Geophysical Research (Space Physics)*, *129*(2), e2023JA032287. doi:10.1029/2023JA032287.

Artemyev, A. V., Zhang, X. J., Zou, Y. et al. (2022b). On the Nature of Intense Sub-Relativistic Electron Precipitation. *Journal of Geophysical Research (Space Physics)*, *127*(6), e30571. doi:10.1029/2022JA030571.

Artemyev, A. V., Zou, Y., Zhang, X.-J. et al. (2024b). Energetic Particle Precipitation in Sub-Auroral Polarization Streams. , *51*(4), e2023GL107731. doi:10.1029/2023GL107731.

Baker, D., Mason, G., Figueroa, O. et al. (1993). An overview of the solar anomalous, and magnetospheric particle explorer (sampex) mission. *IEEE Transactions on Geoscience and Remote Sensing*, *31*(3), 531–541. doi:10.1109/36.225519.

Baker, D. N., Erickson, P. J., Fennell, J. F. et al. (2017). Space Weather Effects in the Earth's Radiation Belts. *Space Science Reviews*, *214*(1), 17. URL: https://doi.org/10.1007/s11214-017-0452-7. doi:10.1007/s11214-017-0452-7.

Berland, G. D., Marshall, R. A., Capannolo, L. et al. (2023). Kinetic Modeling of Radiation Belt Electrons With Geant4 to Study Energetic Particle Precipitation in Earth's Atmosphere. *Earth and Space Science*, *10*(11), e2023EA002987. doi:10.1029/2023EA002987.

Bezanson, J., Edelman, A., Karpinski, S. et al. (2017). Julia: A fresh approach to numerical computing. *SIAM review*, *59*(1), 65–98. URL: https://doi.org/10.1137/141000671.

Burch, J. L., Moore, T. E., Torbert, R. B. et al. (2016). Magnetospheric Multiscale Overview and Science Objectives. , *199*, 5–21. doi:10.1007/s11214-015-0164-9.

Capannolo, L., Li, W., Ma, Q. et al. (2023). Electron Precipitation Observed by ELFIN Using Proton Precipitation as a Proxy for Electromagnetic Ion Cyclotron (EMIC) Waves. , *50*(21), e2023GL103519. doi:10.1029/2023GL103519. arXiv:2309.07539.

Chapman-Smith, K., Seppälä, A., Rodger, C. J. et al. (2023). Observed Loss of Polar Mesospheric Ozone Following Substorm-Driven Electron Precipitation. , *50*(17), e2023GL104860. doi:10.1029/2023GL104860.

Chen, L., Zhang, X.-J., Artemyev, A. et al. (2022). Ducted Chorus Waves Cause Sub-Relativistic and Relativistic Electron Microbursts. , *49*(5), e97559. doi:10.1029/2021GL097559.

Crew, A. B., Spence, H. E., Blake, J. B. et al. (2016). First multipoint in situ observations of electron microbursts: Initial results from the NSF FIREBIRD II mission. *Journal of Geophysical Research (Space Physics)*, *121*(6), 5272–5283. doi:10.1002/2016JA022485.

Distel, J. R., Blair, S. G., Cayton, T. E. et al. (1999). *The combined X-ray dosimeter (CXD) on GPS Block IIR satellites*. Technical Report Tech. Rep. LA-UR-99.

Evans, D. S., & Greer, M. S. (2004). Polar orbiting environmental satellite space environment monitor-2: instrument description and archive data documentation.

Gan, L., Artemyev, A., Li, W. et al. (2023). Bursty energetic electron precipitation by high-order resonance with very-oblique whistler-mode waves. , . doi:10.1029/2022GL101920.

Gan, L., Li, W., Ma, Q. et al. (2022). Dependence of Nonlinear Effects on Whistler-Mode Wave Bandwidth and Amplitude: A Perspective From Diffusion Coefficients. *Journal of Geophysical Research (Space Physics)*, *127*(5), e30063. doi:10.1029/2021JA030063.

Grach, V. S., Artemyev, A. V., Demekhov, A. G. et al. (2022). Relativistic Electron Precipitation by EMIC Waves: Importance of Nonlinear Resonant Effects. , *49*(17), e99994. doi:10.1029/2022GL099994.

Greenspan, A. P. B. . P. J. M., M. E. (1986). *Characteristics of the Thermal Plasma Monitor (SSIES) (Special Sensor for Ions, Electrons, and Scintillation) for the Defense Meteorological Satellite Program (DMSP) Spacecraft S8 through S10*. Technical Report Tech. Rep. AFGL-TR-86-0227. URL: https://apps.dtic.mil/sti/citations/ADA176924.

Hardy, D. A., Schmitt, L. K., Gussenhoven, M. S. et al. (1984). Precipitating electron and ion detectors (SSJ/4) for the block 5D/Flights 6-10 DMSP (Defense Meteorological Satellite Program) satellites: Calibration and data presentation, .

Horne, R. B., Glauert, S. A., Meredith, N. P. et al. (2013). Space weather impacts on satellites and forecasting the Earth's electron radiation belts with SPACECAST. *Space Weather*, *11*, 169–186. doi:10.1002/swe.20023.

Horne, R. B., Thorne, R. M., Glauert, S. A. et al. (2007). Electron acceleration in the Van Allen radiation belts by fast magnetosonic waves. , *34*, 17107. doi:10.1029/2007GL030267.

Kasahara, S., Miyoshi, Y., Yokota, S. et al. (2018). Pulsating aurora from electron scattering by chorus waves. *Nature*, *554*, 337–340. doi:10.1038/nature25505.

King, J. H., & Papitashvili, N. E. (2005). Solar wind spatial scales in and comparisons of hourly Wind and ACE plasma and magnetic field data. , *110*, A02104. doi:10.1029/2004JA010649.

Lam, M. M., Horne, R. B., Meredith, N. P. et al. (2010). Origin of energetic electron precipitation> 30 kev into the atmosphere. *Journal of Geophysical Research: Space Physics*, *115*(A4).

Li, W., & Hudson, M. (2019). Earth's Van Allen Radiation Belts: From Discovery to the Van Allen Probes Era. *Journal of Geophysical Research: Space Physics*, *124*(11), 8319–8351. URL: https://onlinelibrary.wiley.com/doi/abs/10.1029/2018JA025940. doi:10.1029/2018JA025940. _eprint: https://onlinelibrary.wiley.com/doi/pdf/10.1029/2018JA025940.

Lovera, M. (2015). Magnetic satellite detumbling: The b-dot algorithm revisited. In *2015 American Control Conference (ACC)* (pp. 1867–1872). doi:10.1109/ACC.2015.7171005.

Lyons, L. R., & Williams, D. J. (1984). *Quantitative aspects of magnetospheric physics.*.

Mauk, B. H., Fox, N. J., Kanekal, S. G. et al. (2013). Science Objectives and Rationale for the Radiation Belt Storm Probes Mission. , *179*, 3–27. doi:10.1007/s11214-012-9908-y.

Millan, R., Sotirelis, T., Ukhorskiy, A. et al. (2018). The Relativistic Electron Atmospheric Loss (REAL) CubeSat. In *42nd COSPAR Scientific Assembly* (pp. PRBEM.2–3–18). volume 42.

Mironova, I. A., Artamonov, A. A., Bazilevskaya, G. A. et al. (2019). Ionization of the Polar Atmosphere by Energetic Electron Precipitation Retrieved From Balloon Measurements. , *46*(2), 990–996. doi:10.1029/2018GL079421.

Miyoshi, Y., Hosokawa, S., Kurita, S.-I. et al. (2021). Penetration of MeV electrons into the mesosphere accompanying pulsating aurorae. *Scientific Reports*, *11*, 13724. doi:10.1038/s41598-021-92611-3.

Miyoshi, Y., Saito, S., Kurita, S. et al. (2020). Relativistic Electron Microbursts as High-Energy Tail of Pulsating Aurora Electrons. , *47*(21), e90360. doi:10.1029/2020GL090360.

Morley, S. K., Sullivan, J. P., Carver, M. R. et al. (2017). Energetic particle data from the global positioning system constellation. *Space Weather*, *15*(2), 283–289. URL: https://agupubs.onlinelibrary.wiley.com/doi/abs/10.1002/2017SW001604. doi:https://doi.org/10.1002/2017SW001604. arXiv:https://agupubs.onlinelibrary.wiley.com/doi/pdf/10.1002/2017SW001604.

Morley, S. K., Sullivan, J. P., Henderson, M. G. et al. (2016). The global positioning system constellation as a space weather monitor: Comparison of electron measurements with van allen probes data. *Space Weather*, *14*(2), 76–92. URL: https://agupubs.onlinelibrary.wiley.com/doi/abs/10.1002/2015SW001339. doi:https://doi.org/10.1002/2015SW001339. arXiv:https://agupubs.onlinelibrary.wiley.com/doi/pdf/10.1002/2015SW001339.

Mourenas, D., Artemyev, A. V., Zhang, X. J. et al. (2024). Checking Key Assumptions of the Kennel-Petschek Flux Limit With ELFIN CubeSats. *Journal of Geophysical Research (Space Physics)*, *129*(2), e2023JA032193. doi:10.1029/2023JA032193.

Mourenas, D., Artemyev, A. V., Zhang, X.-J. et al. (2021). Electron Lifetimes and Diffusion Rates inferred from ELFIN Measurements at Low Altitude: First Results. *Journal of Geophysical Research: Space Physics*, *126*, e2021JA029757. doi:10.1029/2021JA029757.

Ni, B., Thorne, R. M., Zhang, X. et al. (2016). Origins of the Earth's Diffuse Auroral Precipitation. , *200*, 205–259. doi:10.1007/s11214-016-0234-7.

Nishimura, Y., Bortnik, J., Li, W. et al. (2010). Identifying the Driver of Pulsating Aurora. *Science*, *330*, 81–84. doi:10.1126/science.1193186.

Nishimura, Y., Lessard, M. R., Katoh, Y. et al. (2020). Diffuse and Pulsating Aurora. , *216*(1), 4. doi:10.1007/s11214-019-0629-3.

Oyama, S., Kero, A., Rodger, C. J. et al. (2017). Energetic electron precipitation and auroral morphology at the substorm recovery phase. *Journal of Geophysical Research (Space Physics)*, *122*(6), 6508–6527. doi:10.1002/2016JA023484.

Rich, F. J., & Hairston, M. (1994). Large-scale convection patterns observed by dmsp. *Journal of Geophysical Research: Space Physics*, *99*(A3), 3827–3844. URL: https://agupubs.onlinelibrary.wiley.com/doi/abs/10.1029/93JA03296. doi:https://doi.org/10.1029/93JA03296. arXiv:https://agupubs.onlinelibrary.wiley.com/doi/pdf/10.1029/93JA03296.

Sergeev, V. A., Kubyshkina, M. V., Semenov, V. S. et al. (2023). Unusual Magnetospheric Dynamics During Intense Substorm Initiated by Strong Magnetospheric Compression. *Journal of Geophysical Research (Space Physics)*, *128*(11), e2023JA031536. doi:10.1029/2023JA031536.

Sergeev, V. A., Malkov, M., & Mursula, K. (1993). Testing the isotropic boundary algorithm method to evaluate the magnetic field configuration in the tail. *Journal of Geophysical Research: Space Physics*, *98*(A5), 7609–7620. URL: https://onlinelibrary.wiley.com/doi/abs/10.1029/92JA02587. doi:10.1029/92JA02587. _eprint: https://onlinelibrary.wiley.com/doi/pdf/10.1029/92JA02587.

Sergeev, V. A., Sazhina, E. M., Tsyganenko, N. A. et al. (1983). Pitch-angle scattering of energetic protons in the magnetotail current sheet as the dominant source of their isotropic precipitation into the nightside ionosphere. *Planetary and Space Science*, *31*(10), 1147–1155. URL: https://www.sciencedirect.com/science/article/pii/0032063383901034. doi:10.1016/0032-0633(83)90103-4.

Shen, Y., Artemyev, A. V., Ma, Q. et al. (2022a). Inner Belt Wisp Precipitation Measured by ELFIN: Regimes of Energetic Electron Scattering by VLF Transmitter Waves. *Journal of Geophysical Research (Space Physics)*, *127*(11), e2022JA030968. doi:10.1029/2022JA030968.

Shen, Y., Artemyev, A. V., Runov, A. et al. (2023a). Energetic Electron Flux Dropouts Measured by ELFIN in the Ionospheric Projection of the Plasma Sheet. *Journal of Geophysical Research (Space Physics)*, *128*(9), e2023JA031631. doi:10.1029/2023JA031631.

Shen, Y., Artemyev, A. V., Zhang, X.-J. et al. (2022b). Tens to Hundreds of keV Electron Precipitation Driven by Kinetic Alfvén Waves During an Electron Injection. *Journal of Geophysical Research (Space Physics)*, *127*(8), e30360. doi:10.1029/2022JA030360.

Shen, Y., Artemyev, A. V., Zhang, X.-J. et al. (2023b). Contribution of Kinetic Alfvén Waves to Energetic Electron Precipitation From the Plasma Sheet During a Substorm. *Journal of Geophysical Research (Space Physics)*, *128*(4), e2023JA031350. doi:10.1029/2023JA031350.

Shumko, M., Gallardo-Lacourt, B., Halford, A. J. et al. (2021). A Strong Correlation Between Relativistic Electron Microbursts and Patchy Aurora. , *48*(18), e94696. doi:10.1029/2021GL094696.

Spence, H. E., Caspi, A., Bahcivan, H. et al. (2022). Achievements and Lessons Learned From Successful Small Satellite Missions for Space Weather-Oriented Research. *Space Weather*, *20*(7), e2021SW003031. URL: https://onlinelibrary.wiley.com/doi/abs/10.1029/2021SW003031. doi:10.1029/2021SW003031. _eprint: https://onlinelibrary.wiley.com/doi/pdf/10.1029/2021SW003031.

Stickler, A. C., & Alfriend, K. T. (1976). Elementary Magnetic Attitude Control System. *Journal of Spacecraft and Rockets*, *13*(5), 282–287. doi:10.2514/3.57089.

Swartwout, M. (2023). *University-Class Spacecraft in 2023: More Missions, More Problems?*. Technical Report. URL: https://digitalcommons.usu.edu/smallsat/2023/all2023/43.

Tesema, F., Partamies, N., Tyssøy, H. N. et al. (2020). Observations of Electron Precipitation During Pulsating Aurora and Its Chemical Impact. *Journal of Geophysical Research (Space Physics)*, *125*(6), e27713. doi:10.1029/2019JA027713.

Thorne, R. M. (1980). The importance of energetic particle precipitation on the chemical composition of the middle atmosphere. *Pure and Applied Geophysics*, *118*(1), 128–151. doi:10.1007/BF01586448.

Thorne, R. M. (2010). Radiation belt dynamics: The importance of wave-particle interactions. *Geophysical Research Letters*, *37*(22). URL: https://onlinelibrary.wiley.com/doi/abs/10.1029/2010GL044990. doi:10.1029/2010GL044990. _eprint: https://onlinelibrary.wiley.com/doi/pdf/10.1029/2010GL044990.

Thorne, R. M., Ni, B., Tao, X. et al. (2010). Scattering by chorus waves as the dominant cause of diffuse auroral precipitation. , *467*, 943–946. doi:10.1038/nature09467.

Tsai, E., Artemyev, A., Angelopoulos, V. et al. (2023). Investigating Whistler-Mode Wave Intensity Along Field Lines Using Electron Precipitation Measurements. *Journal of Geophysical Research (Space Physics)*, *128*(8), e2023JA031578. doi:10.1029/2023JA031578.

Tsai, E., Artemyev, A., Ma, Q. et al. (2024). Key factors determining nightside energetic electron losses driven by whistler-mode waves. *Journal of Geophysical Research: Space Physics*, *129*(3), e2023JA032351. URL: https://agupubs.onlinelibrary.wiley.com/doi/abs/10.1029/2023JA032351. doi:https://doi.org/10.1029/2023JA032351. arXiv:https://agupubs.onlinelibrary.wiley.com/doi/pdf/10.1029/2023JA032351. E2023JA032351 2023JA032351.

Tsai, E., Artemyev, A., Zhang, X.-J. et al. (2022). Relativistic Electron Precipitation Driven by Nonlinear Resonance With Whistler-Mode Waves. *Journal of Geophysical Research (Space Physics)*, *127*(5), e30338. doi:10.1029/2022JA030338.

Turunen, E., Kero, A., Verronen, P. T. et al. (2016). Mesospheric ozone destruction by high-energy electron precipitation associated with pulsating aurora. *Journal of Geophysical Research: Atmospheres*, *121*(19), 11–852.

Verronen, P. T., Kero, A., Partamies, N. et al. (2021). Simulated seasonal impact on middle atmospheric ozone from high-energy electron precipitation related to pulsating aurorae. *Annales Geophysicae*, *39*(5), 883–897. doi:10.5194/angeo-39-883-2021.

Wilkins, C., Angelopoulos, V., Runov, A. et al. (2023). Statistical Characteristics of the Electron Isotropy Boundary. *Journal of Geophysical Research (Space Physics)*, *128*(10), e2023JA031774. doi:10.1029/2023JA031774. arXiv:2305.16260.

Xu, W., & Marshall, R. A. (2019). Characteristics of Energetic Electron Precipitation Estimated from Simulated Bremsstrahlung X-ray Distributions. *Journal of Geophysical Research: Space Physics*, *124*(4), 2831–2843. URL: https://onlinelibrary.wiley.com/doi/abs/10.1029/2018JA026273. doi:10.1029/2018JA026273. _eprint: https://onlinelibrary.wiley.com/doi/pdf/10.1029/2018JA026273.

Xu, W., Marshall, R. A., & Tobiska, W. K. (2021). A Method for Calculating Atmospheric Radiation Produced by Relativistic Electron Precipitation. *Space Weather*, *19*(12), e2021SW002735. URL: https://onlinelibrary.wiley.com/doi/abs/10.1029/2021SW002735. doi:10.1029/2021SW002735. _eprint: https://onlinelibrary.wiley.com/doi/pdf/10.1029/2021SW002735.

Xu, W., Marshall, R. A., Tyssøy, H. N. et al. (2020). A generalized method for calculating atmospheric ionization by energetic electron precipitation. *Journal of Geo-*

physical Research: Space Physics, *125*(11), e2020JA028482. URL: https://agupubs.onlinelibrary.wiley.com/doi/abs/10.1029/2020JA028482. doi:https://doi.org/10.1029/2020JA028482. arXiv:https://agupubs.onlinelibrary.wiley.com/doi/pdf/10.1029/2020JA028482. E2020JA028482 10.1029/2020JA028482.

Yahnin, A. G., Yahnina, T. A., Semenova, N. V. et al. (2016). Relativistic electron precipitation as seen by NOAA POES. *Journal of Geophysical Research: Space Physics*, *121*(9), 8286–8299. URL: https://onlinelibrary.wiley.com/doi/abs/10.1002/2016JA022765. doi:10.1002/2016JA022765. _eprint: https://onlinelibrary.wiley.com/doi/pdf/10.1002/2016JA022765.

Yu, Y., Jordanova, V. K., McGranaghan, R. M. et al. (2018). Self-Consistent Modeling of Electron Precipitation and Responses in the Ionosphere: Application to Low-Altitude Energization During Substorms. , *45*(13), 6371–6381. doi:10.1029/2018GL078828.

Zhang, X.-J., Angelopoulos, V., Artemyev, A. et al. (2023a). Temporal Scales of Electron Precipitation Driven by Whistler-Mode Waves. *Journal of Geophysical Research (Space Physics)*, *128*(1), e2022JA031087. doi:10.1029/2022JA031087. arXiv:2211.16579.

Zhang, X.-J., Angelopoulos, V., Mourenas, D. et al. (2022a). Characteristics of Electron Microburst Precipitation Based on High-Resolution ELFIN Measurements. *Journal of Geophysical Research (Space Physics)*, *127*(5), e30509. doi:10.1029/2022JA030509.

Zhang, X.-J., Artemyev, A., Angelopoulos, V. et al. (2022b). Superfast precipitation of energetic electrons in the radiation belts of the Earth. *Nature Communications*, *13*, 1611. doi:10.1038/s41467-022-29291-8.

Zhang, X.-J., Meng, X., Artemyev, A. V. et al. (2023b). Ionospheric Plasma Density Gradients Associated With Night-Side Energetic Electron Precipitation. , *50*(21), e2023GL105630. doi:10.1029/2023GL105630.